Geological Magazine

www.cambridge.org/geo

Original Article

Cite this article: Mehrabi B, Chaghaneh N, Tale Fazel E, and Corfu F. Geology, fluid inclusions and C–O–S–Pb isotopic compositions of the Chahmileh Pb-Zn deposit, Central Iran: Implications for ore genesis. *Geological Magazine* https://doi.org/10.1017/S0016756823000766

Received: 11 March 2023
Revised: 13 November 2023
Accepted: 14 November 2023

Keywords:
Carbonate-hosted Pb-Zn; fluid inclusion; MVT; Chahmileh; Yazd-Anarak Metallogenic Belt; Iran

Corresponding author:
Behzad Mehrabi; Email: mehrabi@khu.ac.ir

Geology, fluid inclusions and C–O–S–Pb isotopic compositions of the Chahmileh Pb-Zn deposit, Central Iran: Implications for ore genesis

Behzad Mehrabi[1], Nafiseh Chaghaneh[1], Ebrahim Tale Fazel[2] and Fernando Corfu[3]

[1]Department of Geochemistry, Faculty of Earth Science, Kharazmi University, Tehran, Iran; [2]Department of Geology, Faculty of Sciences, Bu-Ali Sina University, Hamedan, Iran and [3]Section of Geology and Geophysics, Department of Geosciences, University of Oslo, Oslo, Norway

Abstract

The Chahmileh Pb–Zn deposit, located northwest of the Central Iran Zone, is a sediment-hosted Pb–Zn deposit in the 'Yazd-Anarak Metallogenic Belt'. It is hosted in Middle Triassic carbonate rocks and is mainly controlled by NW-trending faults. The main ore minerals are galena and sphalerite with minor chalcopyrite, pyrite, and quartz, dolomite, along with minor calcite and baryte as gangue minerals. Cerussite, hemimorphite, wulfenite, mimetite, smithsonite, malachite and iron oxy-hydroxides are the main non-sulphide ore minerals. The main styles of mineralization are vein-veinlet, breccia, disseminated and replacement in association with silicification and dolomitization. Microthermometry of fluid inclusions in dolomite and quartz indicates that the ore precipitated from a warm to hot basin-derived saline fluid. Dolomite samples have $\delta^{13}C_{VPDB}$ and $\delta^{18}O_{VSMOW}$ values of −0.99 to +1.99‰ and +20.74 to +25.48‰, respectively, and are plotted in the marine carbonate rocks field. These isotopic values suggest that CO_2 in the hydrothermal fluids mainly originated from marine carbonate rock. The $\delta^{34}S$ values range from +6.3 to +8.2‰ for galena, +5.9 to +6.2‰ for sphalerite, +1.4 to +3.4‰ for chalcopyrite and +15.0 to +17.4‰ for bayite are compatible with a predominant thermochemical sulphate reduction process, and with sulphur sourced from Triassic seawater. Galena samples have a homogeneous Pb isotopic composition that is indicative of a continental crustal reservoir as the main source of lead and probably for the other ore metals. Based on geology, mineralogy, texture and fluid characteristics, the Chahmileh deposit is classified as a carbonate-hosted Mississippi Valley-type deposit.

1. Introduction

Carbonate-hosted Pb–Zn deposits account for a high proportion of the world's Pb–Zn resources and are mainly hosted by siliceous clastic rocks and carbonates that generally show no direct association with igneous rocks (Leach *et al.* 2005, 2010a; Mudd *et al.* 2017). These deposits display a broad range of affiliations to the enclosing host rocks and include stratiform, stratabound, and discordant ores (Leach *et al.* 2005). The Himalayan-Tibetan and Zagros mountain ranges, as the youngest and most extensive continental-collision orogens in the Tethyan domain, host several major sediment-hosted Pb–Zn deposits, including the world-class Jinding, Huoshaoyun, Mehdiabad, and Angouran deposits (Fig. 1; Reynolds & Large, 2010; Rajabi *et al.* 2012, 2015; Hou & Zhang, 2015; Song *et al.* 2017). Many of these deposits were only recently discovered and are poorly documented, especially in Iran. Although more than 300 carbonate-hosted Zn–Pb±Ba deposits/occurrences have been discovered in Iran, there is no general agreement regarding their genetic models of ore formation. It is plausible that these deposits range from sedimentary exhalative (SEDEX) to Mississippi Valley-type (MVT) (Rajabi *et al.* 2012, 2015, 2020). The majority of these deposits are hosted in carbonates of Devonian to Cretaceous age (Ehya, 2014). They largely occur in the Malayer-Esfahan Metallogenic Belt and Yazd-Anarak Metallogenic Belt (YAMB), which is located in the Yazd Block along the northern margin of the Central-East Iranian microcontinent (Rajabi *et al.* 2012) (Fig. 2). Those in the YAMB include many world-class Pb–Zn deposits, such as the Mehdiabad Zn–Pb–Ba–(Cu–Ag) deposit (45.2 Mt oxide @ 7.15% Zn and 2.47% Pb) and 116.5 Mt sulphide (7.3% Zn and 2.3% Pb) (Maghfouri *et al.* 2019, 2020a, 2021). The Yazd block encompasses major Zn-Pb deposits including the Nakhlak Pb–(Ag) (Jazi *et al.* 2017), Darreh-Zanjir Zn–Pb (Maghfouri & Choulet, 2021), Mansourabad-Farahabad Zn–Pb–(Ag) (Maghfouri & Hosseinzadeh, 2018; Maghfouri *et al.* 2020b), Hovzesefid and Anjireh Zn–Pb (Rajabi *et al.* 2012) and Chahmileh Pb–Zn deposits (Technoexport, report, 1984) (Fig. 2). Most Zn-Pb deposits in this region are considered to be

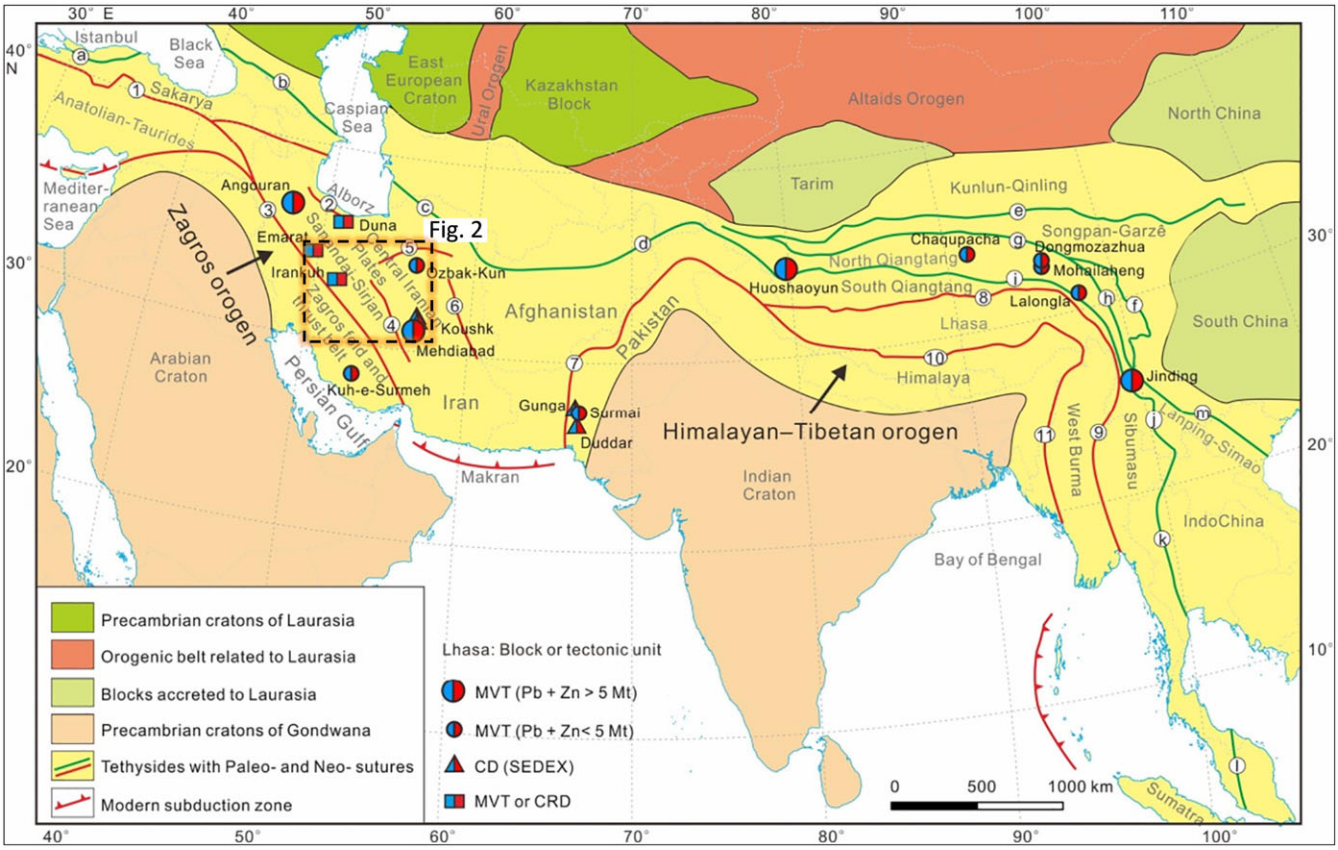

Figure 1. (Colour online) Distribution of the major sediment-hosted Pb–Zn deposits from China to Iran in the Tethyan domain (modified from Hou & Zhang, 2015; Song *et al.* 2019). Paleo-Tethyan sutures (green curves): (a) North Turkey; (b) Lesser Caucasus; (c) Kopet Dagh; (d) North Pamir; (e) Kunlun; (f) Garzê-Litang; (g) western Jinshajiang; (h) eastern Jinshajiang; (i) Longmu Co-Shuanghu; (j) Changning-Menglian; (k) Inthanon; (l) Bentong-Raùb; (m) Ailaoshan. Neo-Tethyan sutures (red curve): 1-Izmir-Ankara-Erzincan; 2-Alborz; 3-Zagros; 4-Nain; 5-Sabzevar; 6-Sistan; 7-Bela-Waziristan-Quetta; 8-Bangonghu-Nujiang; 9-Shan Boundary; 10-Indus-Yarlung-Zangbo; 11-Burma. MVT: Mississippi Valley-Type, CD: Clastic-Dominated, CRD: Carbonate Replacement Deposit.

MVT deposits, formed in a platform carbonate succession, typically in passive margins (Rajabi *et al.* 2012).

The Chahmileh Pb-Zn deposit is located 30 km northeast of Anarak and 12 km south of the Nakhlak Pb-(Ag) deposit, which is one of the oldest mining areas in Iran. Technoexport Co. carried out detailed regional-scale geology and structural investigation in the Anarak area, including the Chahmileh prospect from 1975 to 1985. A detailed exploration program was conducted by Kan-Azin Mining Consultant Company from 2014 to 2017 drilling five boreholes (total length of 1500 m). Previous studies of the deposit focused on geophysical and geochemical exploration features (Technoexport, report, 1984), while the metallogenic mechanism of this deposit remains the subject of considerable debate. However, the sulphur and metal sources, evolution of the ore-forming fluids and the genesis of the deposit remain poorly understood.

In this contribution, we present the results of a comprehensive investigation of the Chahmileh deposit that involves geological field studies, ore mineralogy, fluid inclusions, stable (C–O–S) and radiogenic (Pb) isotope compositions. The aims of the study are to (1) investigate the physical–chemical conditions and metal transport mechanisms; (2) determine the characteristics of the ore-forming fluids and sulphide precipitation mechanism; and (3) evaluate the metal sources and discuss the ore genesis. Studies of the Chahmileh deposit will help to elucidate the ore-forming processes in comparable geologic settings (e.g., MVT and SEDEX), especially where mineralization is associated with subsequent modifications by later hydrothermal activity. In order to facilitate prospecting in the area and improve our understanding of the regional metallogeny in the YAMB, it is crucial to gain further insight into the formation of the Chahmileh deposit.

2. Regional geological setting

The geotectonic history of Iran was affected by the development and evolution of three Tethyan Oceans: The Proto-Tethys Ocean in the Late Neoproterozoic-Cambrian (Pan-African orogeny), the Paleo-Tethys Ocean in the Paleozoic (Cimmerian orogeny) and the Neo-Tethys Ocean during the Mesozoic and Cenozoic (Alpine orogeny) (Bagheri & Stampfli, 2008). The Chahmileh Pb-Zn deposit is situated in the Anarak region, in the northwest corner of the Central Iran Zone (CIZ). The CIZ is the most complicated and largest geological unit in Iran and is an area of continuous continental deformation in response to the ongoing convergence between the Arabian (Gondwanan) and Turan (Eurasian) plates. A series of tectonic events that shaped early evolution of CIZ is associated with the Peri-Gondwanan or Proto-Tethyan episode. At least two further episodes of orogenic activity, one in the Early Triassic and another in the Late Tertiary, affected the CIZ before its final incorporation into the Alpine–Himalayan Belt (Stöcklin, 1974). The CIZ geology consists of Precambrian to Miocene sedimentary rocks, Palaeozoic to Cenozoic ultramafic-acid igneous

https://doi.org/10.1017/S0016756823000766 Published online by Cambridge University Press

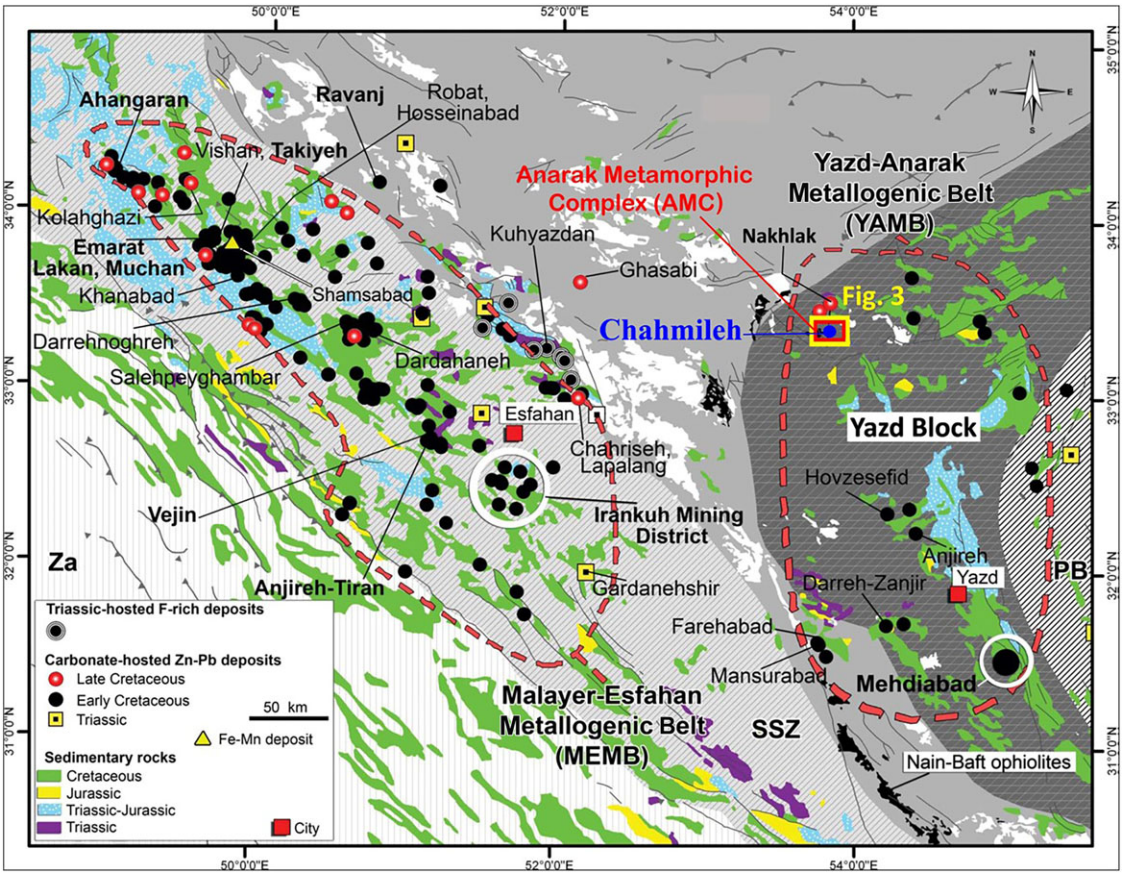

Figure 2. (Colour online) Distribution map of sediment-hosted Zn–Pb (±Ag ± Cu ± Ba) deposits in the Malayer-Esfahan Metallogenic Belt and the Yazd-Anarak Metallogenic Belt (modified after Rajabi *et al.* 2012). Most of the deposits occur on both sides of the Nain-Baft back-arc basin, bordered by the Nain-Baft ophiolites. PB: Posht-e Badam Block, SSZ: Sanandaj–Sirjan Zone, Za: Zagros fold and thrust belt.

rocks and Palaeozoic to Mesozoic metamorphic rocks (Balini *et al.* 2009). The CIZ was a stable platform during the Palaeozoic until Late Triassic movements resulted in the formation of a series of horsts and grabens (Zanchi *et al.* 2009). Major structural trends were created during the Mesozoic when a contiguous platform of the CIZ was divided into small segments (e.g., Stöcklin, 1968; Ramezani & Tucker, 2003). The CIZ consists of three major crustal domains from east to west: the Lut, Tabas, and Yazd Blocks (e.g., Alavi, 1991) which are separated by a series of intersecting regional-scale faults (Berberian, 1981). It is delimited to the north by an E-W trending left-lateral Doruneh (or Great Kavir) fault that interacted with dextral N-S trending faults (Nozaem *et al.* 2013), inherited from the Paleozoic evolution. The Doruneh fault, which is one of the longest and most prominent faults in Iran (Wellman, 1966; Farbod *et al.* 2011), plays an important role in the regional tectonics (Torabi, 2010).

The Chahmileh Pb-Zn deposit is located in the Anarak Metamorphic Complex (AMC) in the CIZ. The AMC consists of intricate polyphase thrust stacks, containing low-grade metapelites, metabasites, and marbles with a greenschist to blueschist metamorphic overprint. It is associated with slivers of ultramafic rocks and metamorphosed-pillow lavas that formed under high-pressure/low-temperature conditions (M Sharkovski *et al.*, report, 1984; Bagheri & Stampfli, 2008; Zanchi *et al.* 2009; Buchs *et al.* 2013; Zanchi *et al.* 2015). It is in tectonic contact with other metamorphic complexes and sedimentary successions of various ages and palaeogeographic affinities. To the west, the Great Kavir-Doruneh fault system represents the contact between AMC and Cretaceous ophiolites that border the Central-East Iranian Microcontinent (Ghasemi & Talbot, 2006). The southern limit of the AMC coincides with the Palaeozoic to Mesozoic sequences of the Yazd block, which geologically are similar to the Alborz region (Wendt *et al.* 2005; Leven & Gorgij, 2006; Zanchi *et al.* 2015). Towards the north, it is bordered by the non-metamorphic Nakhlak ophiolite and associated sedimentary complex (Balini *et al.* 2009). Sedimentary rocks found in the Nakhlak area include a 2400 m-thick forearc succession of turbiditic, shallow-marine and fluvial deposits (i.e. 'Nakhlak Group' after Balini *et al.* 2009) recording the erosion of a nearby volcanic arc and metamorphic basement, presumably the AMC (Bagheri & Stampfli, 2008; Balini *et al.* 2009; Zanchi *et al.* 2009). Forearc tectonic features of the Nakhlak area are characterized by supra-subduction and boninitic gabbros dated at ~387 Ma (S Bagheri, unpub. PhD thesis, Univ. Lausanne, 2007; Bagheri & Stampfli, 2008). The contact between the AMC and Nakhlak complex is not exposed, so the timing relationship between them is unclear (Balini *et al.* 2009; Zanchi *et al.* 2009). To the east of the AMC, the Jandaq Metamorphic Complex, containing medium to possibly high-grade)likely Carboniferous or pre-Carboniferous(metamorphic rocks, was intruded by early Mesozoic granites and pegmatite (Bagheri & Stampfli, 2008; Berra *et al.* 2017).

The AMC is composed of several subunits, including the Morghab, Chah Gorbeh, Patyar, Lakh Marble, Palhavand Gneiss, Doshak and Bayazeh complexes (Fig. 3; M Sharkovski *et al.*, report,

https://doi.org/10.1017/S0016756823000766 Published online by Cambridge University Press

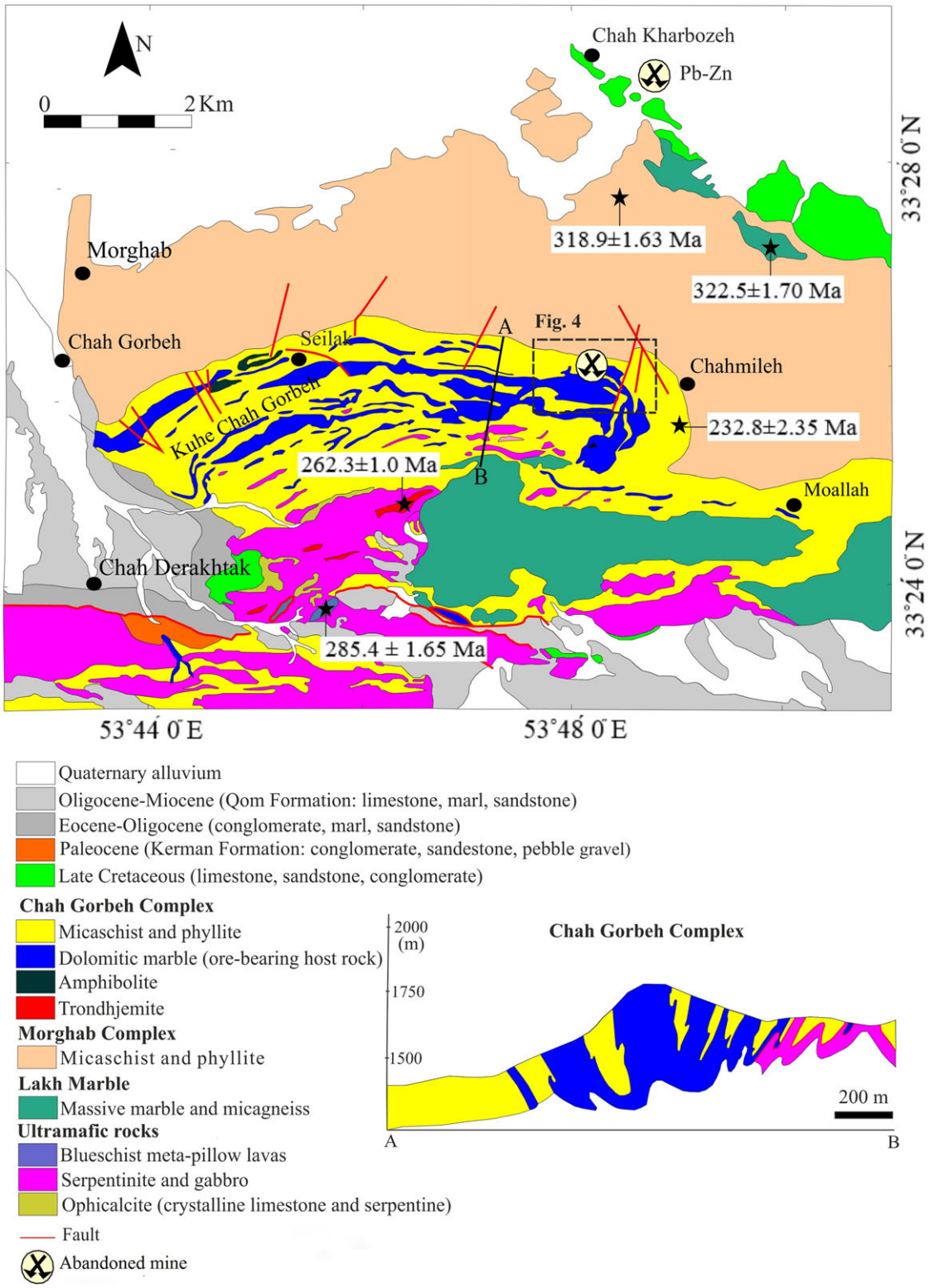

Figure 3. (Colour online) Geological map of the northern part of the Anarak Metamorphic Complex with N–S trending cross-section (A-B) (modified after Zanchi *et al.* 2015). Radiometric ages of various rocks are adopted from Bagheri & Stampfli (2008).

1984; Bagheri & Stampfli, 2008; Zanchi *et al.* 2009, 2015). They display heterogeneous structural and metamorphic histories and are cross-cut by small mafic to felsic intrusive bodies, mainly trondhjemite dykes and Late Permian stocks (Bagheri & Stampfli, 2008). The AMC is interpreted to be an allochthonous crustal fragment that was part of an accretionary wedge developed along the southern Eurasian margin, in the hanging wall of the Palaeo-Tethys subduction zone (Zanchi *et al.* 2015) and preceding the collision of the Iran plate with Eurasia during the Cimmerian orogenic event (Zanchetta *et al.* 2017).

https://doi.org/10.1017/S0016756823000766 Published online by Cambridge University Press

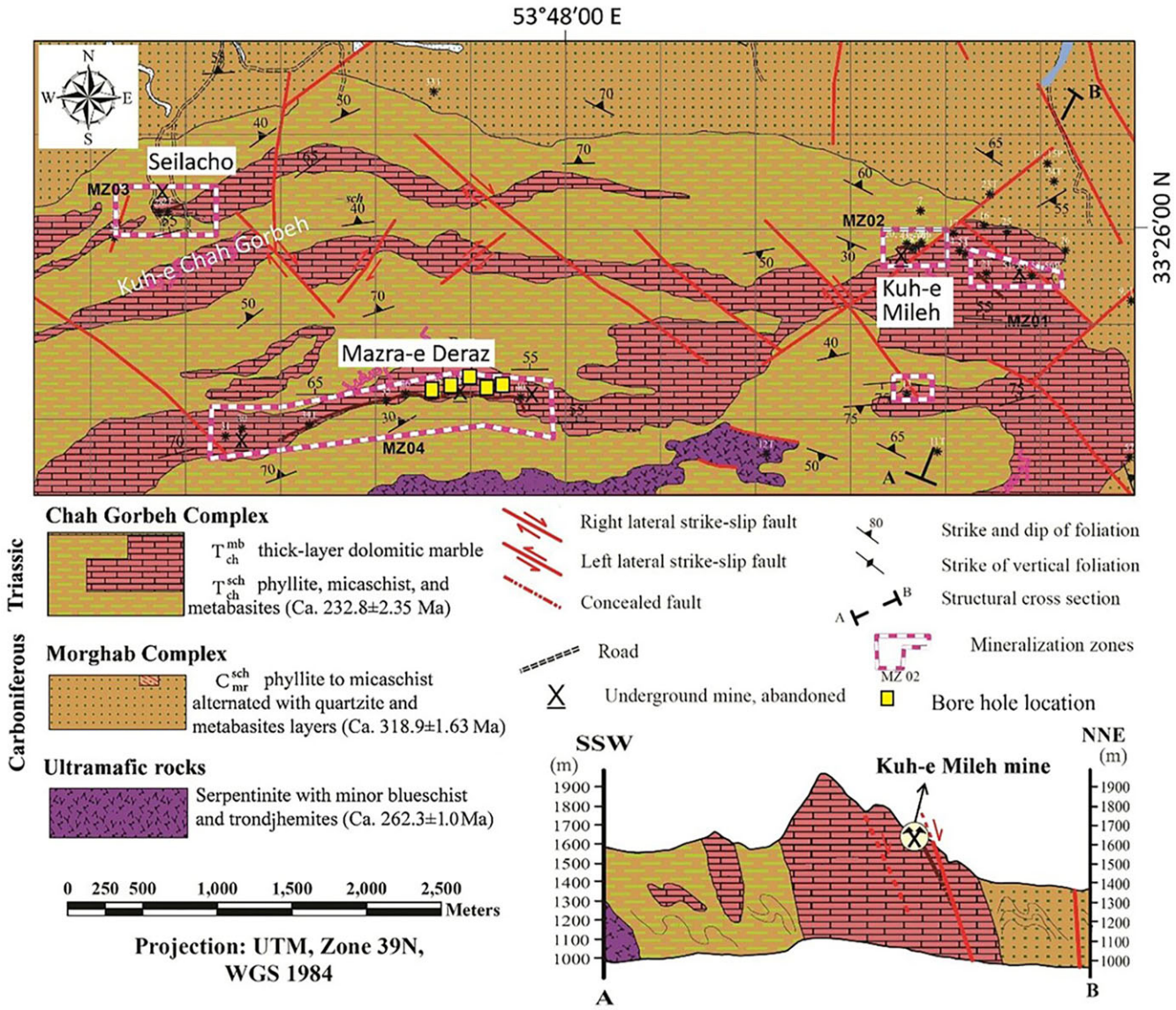

Figure 4. (Colour online) A simplified geological map of the Chahmileh Pb-Zn deposit showing the mineralization and dolomitic marble host rock of the Chah Gorbeh Complex (modified after Kan-Azin Mining Consultant Company, report, 2014).

The Anarak complex is cross-cut by an array of E-W and NW-SE striking faults that are truncated to the NW against the southern terminal branch of the Doruneh fault system. These faults cut the Cenozoic sedimentary deposits that overly the metamorphic and ultramafic basement. The main structure in the area is the 45 km long, E-W to NNW-SSE striking, SW dipping Ashin thrust fault, which juxtaposes the hanging wall of the metamorphic basement, and ultramafic mantle rocks of the AMC with the Cenozoic sedimentary and volcanic rocks in its footwall (Javadi *et al.* 2015).

3. Ore deposit geology

The Chahmileh area mainly consists of ultramafic rocks and the Carboniferous to Permo-Triassic low-grade metamorphic sequence of the Morghab and Chah Gorbeh complexes (Fig. 4). Ultramafic rocks are composed of coarse-grained hornblende gabbro in close association with serpentinized ultramafic rocks and minor blueschist and small trondhjemite stocks (Fig. 5a). The blueschists have an ocean island basalt geochemical affinity (Bagheri & Stampfli, 2008; Torabi, 2011), whereas the trondhjemites have a supra-subduction origin and yielded a U-Pb zircon age of 262.3 ± 1.0 Ma (Bagheri & Stampfli, 2008; Torabi, 2012).

The Morghab Complex is present throughout the area in close association with the Chah Gorbeh Complex (Figs. 3, 4). It consists of a monotonous assemblage of low-grade metapelites, varying from phyllite to mica schist alternating with quartzite and metabasites layers, and thin intercalations of marble (Fig. 5b). Garnet-biotite-mica schists locally occur close to the Chah Karbouzeh area (Fig. 3). Bagheri and Stampfli (2008) reported an Ar-Ar age of 318.9 ± 1.63 Ma for metamorphism of the Morghab Complex.

The Chah Gorbeh Complex consists of two units: (1) quartzite-rich phyllite, micaschist and metabasites and (2) interlayers of thick-bedded dolomitic marble (Figs. 3, 4, 5c–e). These rock units are very similar in composition to those in the Morghab Complex. Meta-cherts occur within the marble layers and along their

https://doi.org/10.1017/S0016756823000766 Published online by Cambridge University Press

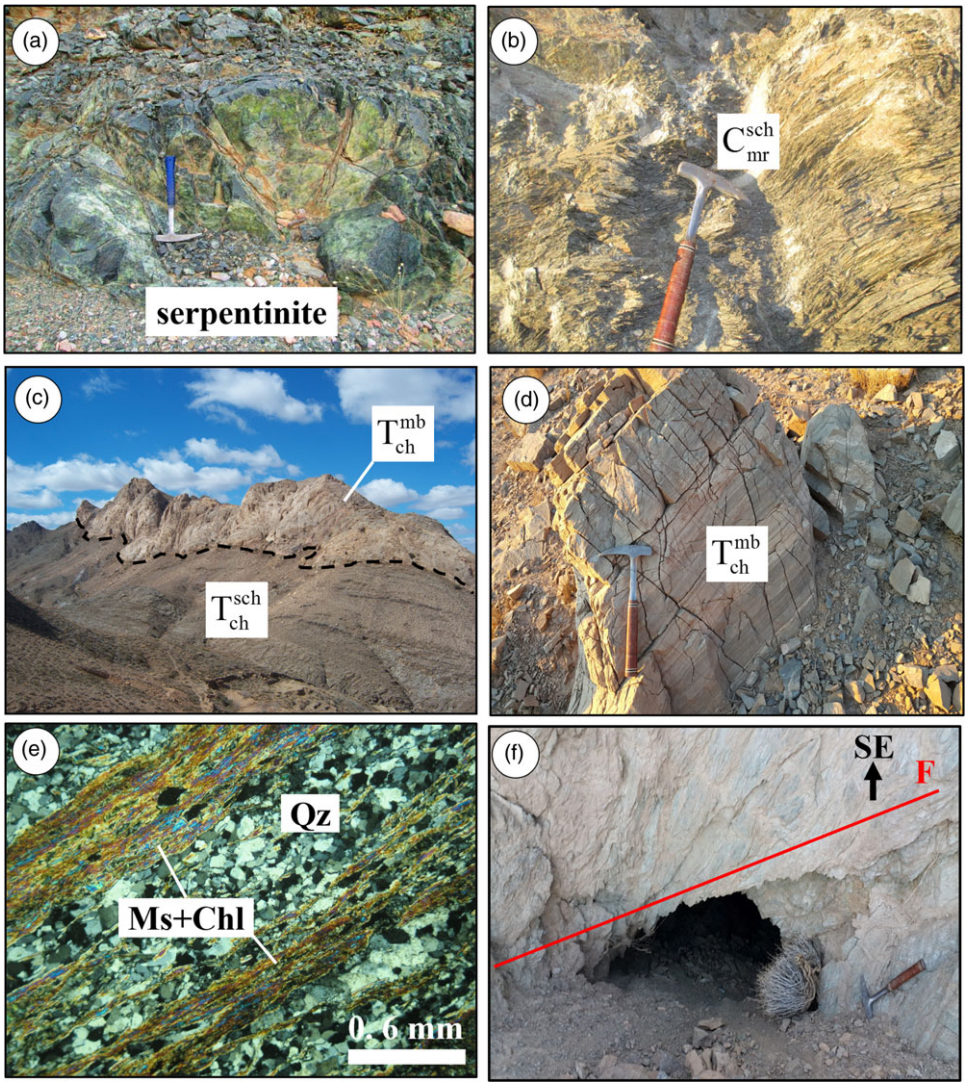

Figure 5. (Colour online) Field photographs and photomicrograph of representative rocks at the Chahmileh. (a) Serpentinite southeast of Mazra-e Deraz, (b) Quartz veins in micaschist and phyllite of the Morghab Complex (C_{mr}^{sch}), (c) Muscovite chlorite schist unit (T_{ch}^{sch}) and its contact with dolomitic marble (T_{ch}^{mb}) of the Chah Gorbeh Complex, (d) Dolomitic marble (T_{ch}^{mb}) of the Chah Gorbeh Complex; e Muscovite chlorite schist, showing nematoblastic and granoblastic textures, f NW-trending normal fault in the Kuh-e Mileh tunnel. F: Fault.

contacts. Metabasite, which was metamorphosed to the greenschist facies is intercalated with this unit. The Chah Gorbeh Complex is generally concordant with the Morghab Complex, at least around Chah Gorbeh mountain (Fig. 3). Zanchi *et al.* (2015) reported a tectonic contact with the Lakh Marble in the Doldol mountain (southern Anarak) and around the Chah Gorbeh mountain (Fig. 3). Metabasalt and meta-greywacke samples from the Chah Gorbeh Complex yield an age of 232.8 ± 2.35 Ma using Ar-dating of stilpnomelane (Bagheri & Stampfli, 2008; Buchs *et al.* 2013). Previous K-Ar radiometric dating on mineral separates and bulk rock samples range in age from 420 to 208 Ma with a main cluster between 375 and 300 Ma (M Sharkovski *et al.*, report, 1984).

In the Chahmileh prospect area, NW-trending faults dipping towards the NE are the most prominent structural feature (Fig. 5f) in association with NE- to N-trending faults that dip steeply to the NW or SE. These normal faults have a moderate sinistral strike-slip component. Exposed reverse faults in the Mazra-e Deraz area displaced ultramafic units over the younger sequences.

A thick-layered dolomitic marble unit of the Chah Gorbeh Complex with a maximum exposed thickness of 700 m is the main host rock of the Chahmileh Pb–Zn deposit (Fig. 4). Field evidence indicates that ore mineralization is controlled mainly by faults (Fig. 6a, b). In the study area, there are three zones of Pb-Zn mineralization, Kuh-e Mileh, Seilacho and Mazra-e Deraz.

Kuh-e Mileh is the largest deposit, located in the eastern part of the Chahmileh area (Fig. 4), with a reserve of ~1 Mt @ 2.15% Pb + Zn (Kan-Azin Mining Consultant Company, report, 2015). The ore body is stratabound with a lenticular shape. Mineralization mainly occurs in structurally controlled open-space fillings and locally as a replacement of the host rock where breccia- and vein-type ores are the major style of mineralization (Fig. 6c–f). Breccia clasts are poorly sorted, angular to subangular in shape and range in size from a few centimetres to a few tens of centimetres in size. Quartz, galena and haematite are the main minerals in the breccia cement (Fig. 6e, f). Disseminated and open-space filling is prominent and likely formed by hydrothermal fluid percolation or replacement. In some cases, disseminated galena and pyrite fill the open-space between dolomitic crystals in the altered host rock. Massive ore is not common and is only rarely found as thick veins of galena (Fig. 6d). Ore mineral assemblages are relatively simple and are dominated by galena and sphalerite with minor amounts of chalcopyrite and pyrite. Oxidation and weathering processes lead to the dissolution and alteration of sulphide minerals and development of non-sulphide ore that consists of cerussite,

https://doi.org/10.1017/S0016756823000766 Published online by Cambridge University Press

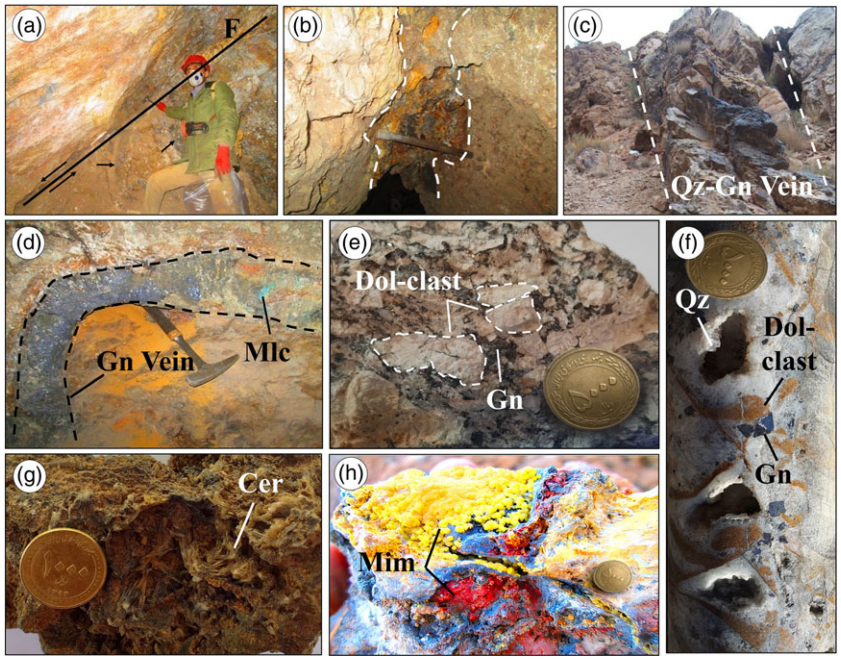

Figure 6. (Colour online) Photograph showing ore textures and mineralization features at the Chahmileh deposit. (a) Mineralization located in the footwall of the NW-trending normal fault (F), (b) Mineralization in fault zone, (c) Quartz-galena vein hosted in the dolomitic marble unit (T_{ch}^{mb}) of the Chah Gorbeh Complex, (d) Vein-type galena mineralization associated with minor malachite at the Kuh-e Mileh tunnel, (e) Clasts of dolomitic host rock replaced by galena, (f) Dolomite breccia clasts associated with quartz-galena, (g) Cerussite and (h) Mimetite in the oxidized zone. Abbreviation of minerals adopted from Warr (2021): Cer: Cerussite, Dol: Dolomite, Gn: Galena, Mlc: Malachite, Mim: Mimetite, Qz: Quartz.

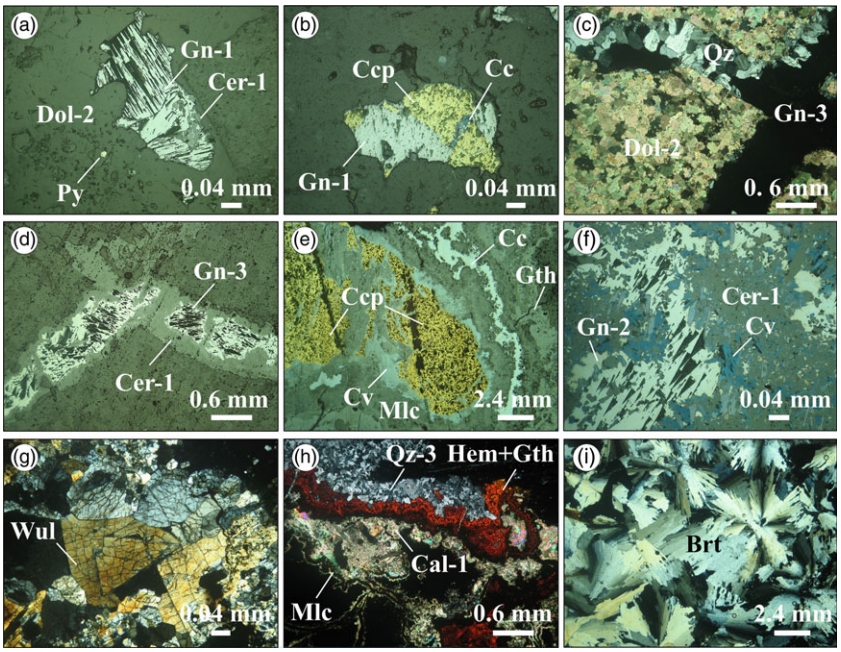

Figure 7. (Colour online) Photomicrographs of sulphide, non-sulphide, and gangue minerals at the Chahmileh deposit. (a) Disseminated pyrite accompanied by subhedral disseminated galena (Gn-1) partly replaced by cerussite (Crt-1) (PPL), (b) Intergrowth of chalcopyrite, galena (Gn-1), and chalcocite replacing chalcopyrite (PPL), (c) Galena (Gn-3)-quartz (Qz-2) veinlet within dolomitic marble (Dol-2) (XPL), (d) Conjugate galena (Gn-3) veinlets (PPL), (e) Secondary minerals formed on rims of chalcopyrite (PPL), (f) Covellite bladed crystals and cerussite (Crt-1) replacing galena (Gn-2) (PPL), (g) Wulfenite crystals (XPL), (h) Banded haematite+goethite associated with calcite (Cal-1) and malachite (XPL), (i) Acicular baryte (XPL). Abbreviation of minerals adopted from Warr (2021): Brt: Baryte, Cal: Calcite, Ccp: Chalcopyrite, Cc: Chalcocite, Cer: Cerussite, Cv: Covellite, Dol: Dolomite, Gth: Goethite, Gn: Galena, Hem: Haematite, Mlc: Malachite, Py: Pyrite, Qz: Quartz, Wul: Wulfenite.

hemimorphite, mimetite, wulfenite, smithsonite, malachite and iron oxy-hydroxides (Fig. 6g, h).

Galena is the main ore mineral and is characterized by medium- to coarse-grained (0.1 mm to >1 cm in size), subhedral to euhedral crystals mainly as disseminations (Figs. 7a, b, 10c), veins and veinlets (Fig. 7c, d) and as grains in breccia (Fig. 7f). Disseminated galena formed at the same time as intergrowths with other sulphides (Fig. 7b). Sphalerite is found as subhedral to anhedral inclusions (40–60 μm in size) within galena crystals (Fig. 8a, i) whereas chalcopyrite is a minor ore mineral and occurs as disseminated, medium to coarse-grained (0.1–3 mm), subhedral to anhedral crystals. Locally, chalcopyrite was replaced by secondary covellite, chalcocite, goethite and malachite (Fig. 7b, e). Pyrite is a minor phase and occurs as euhedral and/or subhedral fine grains (2–5 μm in size), disseminated in the host rock and among other ore minerals (Fig. 7a) where it is partially or completely altered to goethite.

Supergene minerals are divided into two categories: sulphide and non-sulphide minerals. Covellite is the most abundant supergene sulphide mineral where it occurs as bladed crystals (10–200 μm in size) and is derived from the alteration of chalcopyrite along fractures (Fig. 7e, f). Cerussite, the most common oxidized lead mineral in the deposit, occurs as fine-grained cerussite that replaced galena (Figs. 7a, d, f, 8a–c, i) and coarse-grained cerussite filling open fractures and cavities (Fig. 8e, f). Mimetite ($Pb_5(AsO_4)_3Cl$) occurs in the supergene mineralization and is spatially associated with

https://doi.org/10.1017/S0016756823000766 Published online by Cambridge University Press

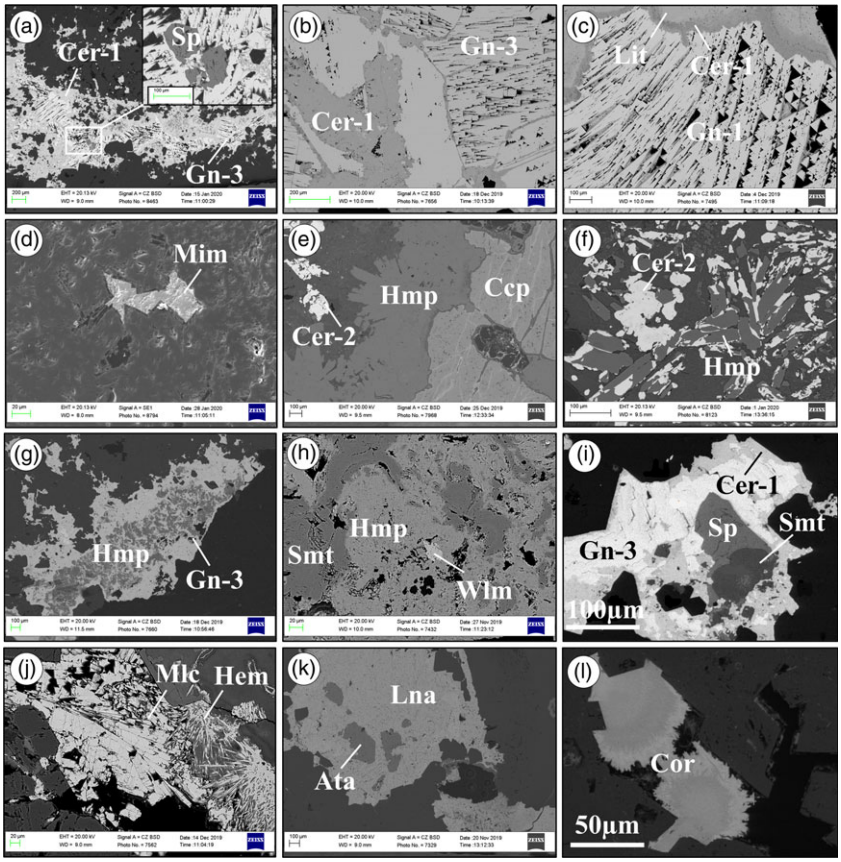

Figure 8. (Colour online) BSE images of sulphide and non-sulphide minerals at the Chahmileh deposit. (a) Sphalerite inclusions in galena (Gn-3) and replacement of cerussite (Crt-1) on galena rims, (b) Galena (Gn-3) cleavage and cerussite (Crt-1) replacement, (c) Galena (Gn-1) boundary replacement by cerussite (Crt-1) and litharge, (d) Mimetite with open-space filling texture in dolomitic marble, (e) Chalcopyrite with platy hemimorphite and disseminated cerussite (Crt-2), (f) Platy euhedral crystals of hemimorphite and second generation of cerussite (Cer-2), (g) Hemimorphite inclusions within galena (Gn-3), (h) Assemblage of hemimorphite, willemite and colloform smithsonite, (i) Sphalerite inclusions within galena (Gn-3) and sphalerite replacement by smithsonite, (j) Needle shape radial haematite and pyramidal malachite as open-space filling texture, (k) Atacamite inclusions within linarite, (l) Coronadite subhedral crystals. Abbreviation of minerals adopted from Warr (2021): Ata: Atacamite, Ccp: Chalcopyrite, Cer: Cerussite, Cor: Coronadite, Dol: Dolomite, Gn: Galena, Hem: Haematite, Hmp: Hemimorphite, Lna: Linarite, Mlc: Malachite, Lit: Litharge, Mim: Mimetite, Qz: Quartz, Smt: Smithsonite, Sp: Sphalerite, Wlm: Willemite.

secondary Pb minerals (Fig. 8d). Wulfenite ($PbMoO_4$) is associated with cerussite as open-space filling textures (Fig. 7g), and is likely an oxidation product of molybdenum in galena (e.g., Graton & Harcourt, 1935; Takahashi, 1960). Supergene Zn minerals are generally less common than secondary Pb minerals and consist of hemimorphite and smithsonite with minor, hydrozincite and willemite. Hemimorphite has a medium to coarse-grained, elongate shape, relatively high relief and distinct longitudinal cleavage, with a mosaic-type and blocky texture, up to 3 mm in size (Fig. 8e–h). Smithsonite is generally less abundant than hemimorphite and formed in open-space cavities in the carbonate rocks where it replaced sphalerite (Fig. 8h, i). Haematite occurs in banded, scaffold, reticulate, colloform, needle and radial textures (Figs. 7h, 8j). Other supergene minerals associated with the non-sulphide ore identified by scanning electron microscopy and energy dispersive spectroscopy (SEM-EDS) are litharge (PbO) (Fig. 8c), minium (Pb_3O4), linarite ($PbCu[(OH_2)\text{-}SO_4]$ (8k), atacamite ($Cu_2Cl(OH)_3$) (8k), coronadite (8l), malachite (Fig. 8j), azurite, cuprite, chrysocolla and magnetite.

Gangue minerals are dominated by quartz, dolomite, calcite and baryte. Quartz typically occurs as fine to coarse-grained (< 20 µm to >1 cm in size), anhedral to euhedral crystals and cryptocrystalline to holocrystalline forms, and locally contains carbonate inclusions. Dispersed platy and prismatic crystals, subparallel and radial growths and swallow-tail bundles and stellate aggregates of baryte, a few mm to cm in length, fill open spaces and vugs in the host rocks (Fig. 7i). Calcite occurs as a minor gangue mineral formed during the main and late-stages of mineralization.

Based on mineral assemblages, ore textures and cross-cutting relationships, the ore-forming process at the Chahmileh deposit can be divided into three stages: (1) sedimentary and diagenetic stage (pre-ore stage), (2) hydrothermal mineralization (main-ore stage) and (3) post-ore stage (Fig. 9).

The sedimentary and diagenetic stage (pre-ore stage) is represented by dolomite crystals formed during diagenesis, prior to the dolomitization associated with the main-ore stage. This stage is locally difficult to identify due to hydrothermal overprinting by the main-stage minerals. The pre-ore stage is also associated with the formation of dolomite that replaced calcite in limestones, a process that generates porosity for further fluid flow and deposition of other minerals. The sedimentary and diagenetic stage also contains very fine-grained disseminated pyrite.

Hydrothermal mineralization (main-ore stage) is the main ore-forming stage in terms of both volume and grade.

Post-ore stage includes barren calcite, quartz or dolomite veins and veinlets, which cross-cut stages 1 and 2 and fill secondary fractures and voids, together with supergene ores, derived from the oxidation of primary ores in surficial environments.

Hydrothermally altered rocks occur together with sulphide mineralization mainly along and/or near faults or fractures, indicating that both the mineralized and altered rocks are structurally controlled. Dolomitization and silicification are the main types of alteration, where it is commonly accompanied by brecciation. Based on grain size, shape and colour, dolomite can be classified into three types (Dol-1, Dol-2 and Dol-3). Dol-1, which mainly occurs as cement, consists of a mosaic of grey unimodal, nonplanar dolomite crystals less than 20 µm size, formed by the late diagenetic replacement of limestone (Fig. 10a). The most pervasive type of dolomite, Dol-2, is characterized by medium- to coarse-grained, subhedral to euhedral crystals. Euhedral, poly-modal crystals are rarely observed but are characterized by cloudy centres and clear rims. This zonation reveals fluctuations in the

https://doi.org/10.1017/S0016756823000766 Published online by Cambridge University Press

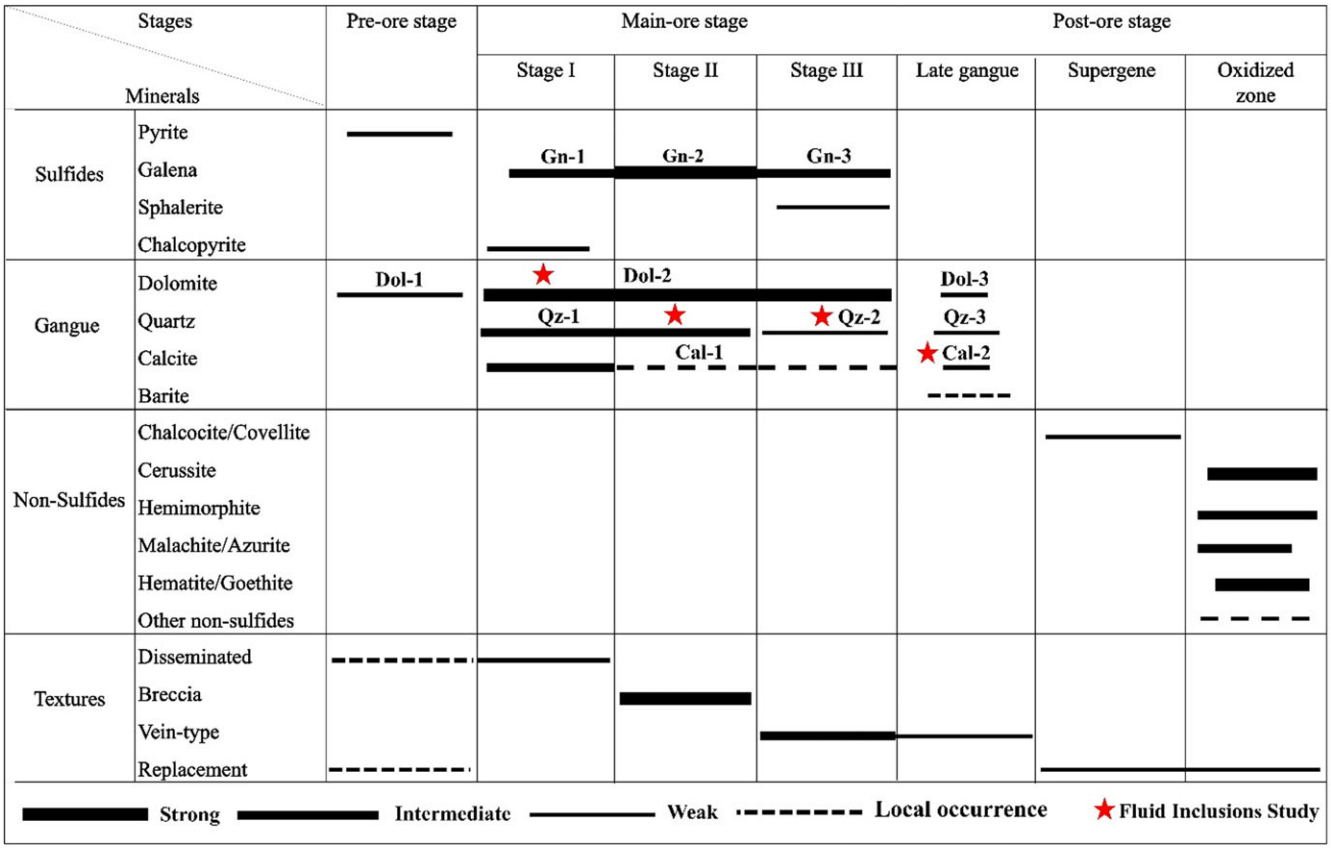

Figure 9. (Colour online) Paragenetic sequence of the Chahmileh deposit, thickness of line representing the minerals frequency.

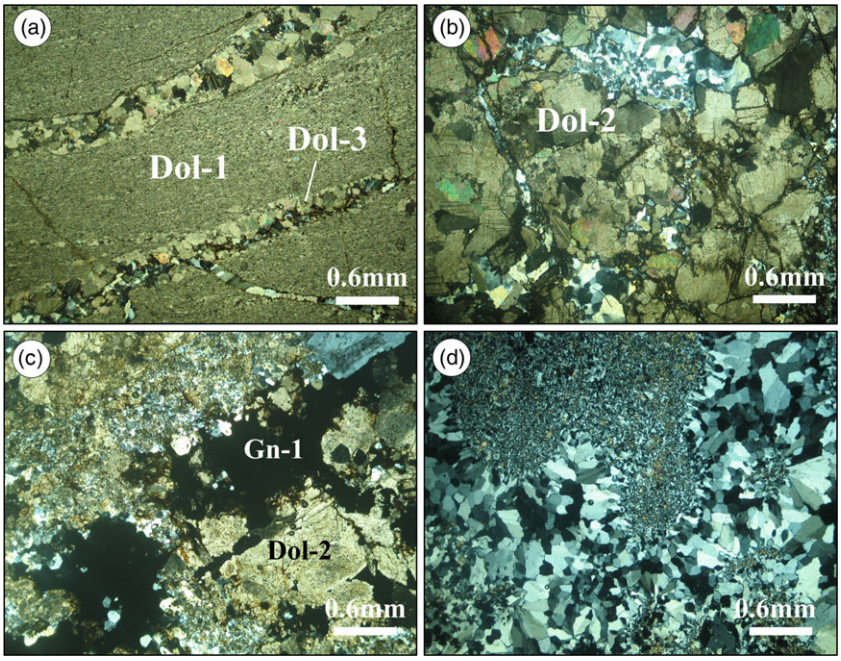

Figure 10. (Colour online) Photomicrographs of various alterations at the Chahmileh deposit. (a) Type I (Dol-1) and III dolomite (Dol-3) (XPL), (b) Medium to coarse-grained, subhedral to euhedral type II dolomite (Dol-2) (XPL), (c) The second type of dolomite (Dol-2), which is replaced by disseminated galena (Gn-1) (XPL) (d) Silicification alteration (XPL). Abbreviation of minerals adopted from Warr (2021): Dol: Dolomite, Gn: Galena.

chemistry of the dolomitising fluid. The Dol-2 intercrystalline porosity is infilled by galena and quartz and/or is replaced by galena and quartz (Fig. 10b, c). The Dol-3 occurs as veins containing anhedral, nonplanar and medium-grained crystals (Fig. 10a).

Silicification formed massive to vuggy bodies of microcrystalline to cryptocrystalline quartz generally as a cement in mineralized breccia or individual veins. There is a close spatial association between sulphides and quartz, with sulphides

https://doi.org/10.1017/S0016756823000766 Published online by Cambridge University Press

formed as disseminations and veinlets within the quartz bodies (Fig. 10c, d).

4. Sampling and analytical methods

One hundred and fifty representative samples of the Pb–Zn ore and host rocks were collected, and after preparing thin and polished sections, they were examined by a ZEISS Axioplan-2 transmitted and reflected light microscope. After ore petrography, sulphide and non-sulphide minerals were checked by SEM-EDS using a VP-SEMEDS ZEISS 3700 at the Central Laboratory of Kharazmi University (Tehran, Iran). Mineralogical abbreviations used throughout the manuscript are according to Warr (2021).

4.1. Fluid inclusion analysis

Petrographic and microthermometric studies were carried out on fluid inclusions in dolomite ($n = 3$) and quartz ($n = 2$) from the main-ore stage and late calcite veins ($n = 1$) of the post-ore stage. Microthermometry of fluid inclusions was carried out in the Geochemistry Department of Kharazmi University (Tehran, Iran), using a Linkam THMS600 heating–freezing stage (−190 to +600 °C) mounted on a ZEISS Axioplan-2 microscope. Temperature was calibrated using Synflinc synthetic fluid inclusion standards. The estimated accuracy is ±0.5 °C for temperatures below 100 °C and ±1.0 °C for temperatures in the range of 100–600 °C. Heating/cooling rates were restricted to 5–10 °C/min and were reduced to 0.1–0.5 °C/min near phase transformations. Freezing measurements were conducted before heating measurements. The following parameters were measured in aqueous inclusions (based on the nomenclature of Diamond, 2003); first ice-melting temperature (T_{fm}), final ice-melting temperature (Tm_{ice}) and total homogenisation temperature (Th). Salinity is expressed as wt.% NaCl eq. calculated from (Tm_{ice}) using the equations of Bodnar (1993) for aqueous inclusions. Molar volumes, compositions and density were calculated using the FLINCOR software (Brown, 1989).

4.2. Stable isotope analysis

Eleven dolomite samples of the main-ore stage, deposited contemporaneously with galena, were analysed for carbon ($\delta^{13}C$) and oxygen ($\delta^{18}O$) isotopic composition. Samples were analysed using a Kiel III device connected to a Finnigan MAT 252 isotope ratio mass spectrometer in the Department of Geological Sciences at the University of Florida. Carbon isotope data expressed in the δ notation in per mil (‰) relative to Vienna Pee Dee Belemnite (VPDB), whereas those for oxygen isotopes are reported relative to Vienna Standard Mean Ocean Water (VSMOW). The precision of the technique was measured with an internal standard of Carrera Marble calibrated with NSB-19 and found to be ± 0.04‰ for $\delta^{18}O$ and ± 0.08‰ for $\delta^{13}C$.

Eight sulphide samples including galena ($n = 4$), chalcopyrite ($n = 2$) and sphalerite ($n = 2$) from the main-ore stage and baryte ($n = 2$) from the post-ore stage were selected for sulphur isotope analyses. Separates of sulphide minerals were prepared by handpicking under a binocular microscope to achieve a purity of > 99%. The $\delta^{34}S$ values were measured in SO_2 gas using a continuous-flow gas-ratio mass spectrometer (Thermo Quest Finnigan Delta Plus XL) at the Environmental Isotope Laboratory of Arizona University. Sulphur isotopic composition was determined after combustion at 1030 °C in oxygen (O_2 or V_2O_5) using an elemental analyser (Costech) coupled to the mass spectrometer. Standardization was based on international standards OGS-1 and NBS123, and several other sulphide and sulphate materials that have been compared between laboratories. The data are presented in delta (δ) notation as per mill (‰) deviations relative to the Vienna Canyon Diablo Troilite (VCDT) standard for sulphur. Calibration is linear in the range −10 to +30‰. Precision is estimated to be ± 0.15‰ or better (1σ), based on repeated measurement of internal standards.

4.3. Lead isotope analysis

Lead isotope compositions of galena ($n = 2$, stage I; $n = 2$, stage II and $n = 2$, stage III of main-ore stage) were measured at the University of Oslo. Lead was leached from the samples with dilute acid, mixed with phosphoric acid and silica gel and loaded directly on outgassed Re filaments. Ratios were measured by thermal ionization mass spectrometry on a MAT262 instrument using multiple Faraday cups in static mode (Corfu, 2004). Data are corrected for fractionation of 0.10 ± 0.06% per atomic mass unit. Reproducibility of the fractionation (based on NBS982) is propagated into the uncertainty of the corrected ratios. The Isoplot 4.1 programme was used for plotting Pb-isotope results.

5. Results

5.1. Fluid inclusions petrography

Fluid inclusions were studied in dolomite (Dol-2), quartz (Qz-1 and Qz-2) and calcite (Cal-2) from the main-ore and post-ore stages. No workable fluid inclusions were identified in minerals from the pre-ore stage. Based on the criteria of Roedder (1984), there are both primary and secondary fluid inclusions in the samples. Fluid inclusions that are clustered or isolated are considered primary, whereas those aligned along microfractures in transgranular trails were designated as secondary, which are mostly less than 2 μm in size. Only primary fluid inclusions associated with the main and post-ore stages of mineralization processes were selected for fluid inclusion studies. Fluid inclusion shapes are rectangular, elliptical, circular, rod-shaped or elongated and rarely irregular. Diameter of the investigated inclusions was in range of 5–30 μm, mostly around 5–15 μm. With exception of a few single-phase aqueous and vapour inclusions, almost all inclusions are two-phase (L + V), liquid-rich with a 10–20 volume per cent of vapour bubble that homogenized to liquid upon heating (Fig. 11).

5.2. Microthermometry

Microthermometric data of the primary fluid inclusions are listed in Table 1 and shown in Fig. 12. The T_{fm} of primary inclusions in dolomite crystals from the main-ore stage I varies from −35.0 to −29.0 °C (avg. = −31.4 °C, $n = 24$), suggesting the presence of appreciable amount of $CaCl_2$ in addition to NaCl and KCl (Van den Kerkhof & Hein, 2001). Inclusions homogenized into the liquid phase between 133.0 and 248.0 °C (avg. = 205.3 °C, $n = 27$). The Tm_{ice} value for these inclusions varies from −17.7 to −12.3 °C (avg. = −14.3 °C, $n = 27$), corresponding to a salinity of 16.2 to 20.8 wt.% NaCl eq. (avg. = 18.0 wt.%, $n = 27$). Density of these inclusions is 0.89−1.04 g/cm^3.

Primary inclusions in quartz crystals from the main-ore stage II show T_{fm} of −38.0 to −32.0 °C (avg. = −34.3 °C, $n = 17$), suggesting the presence of appreciable amounts of $CaCl_2$ in addition to NaCl and KCl (Van den Kerkhof & Hein, 2001). Inclusions homogenized into the liquid phase between 136.0 and

https://doi.org/10.1017/S0016756823000766 Published online by Cambridge University Press

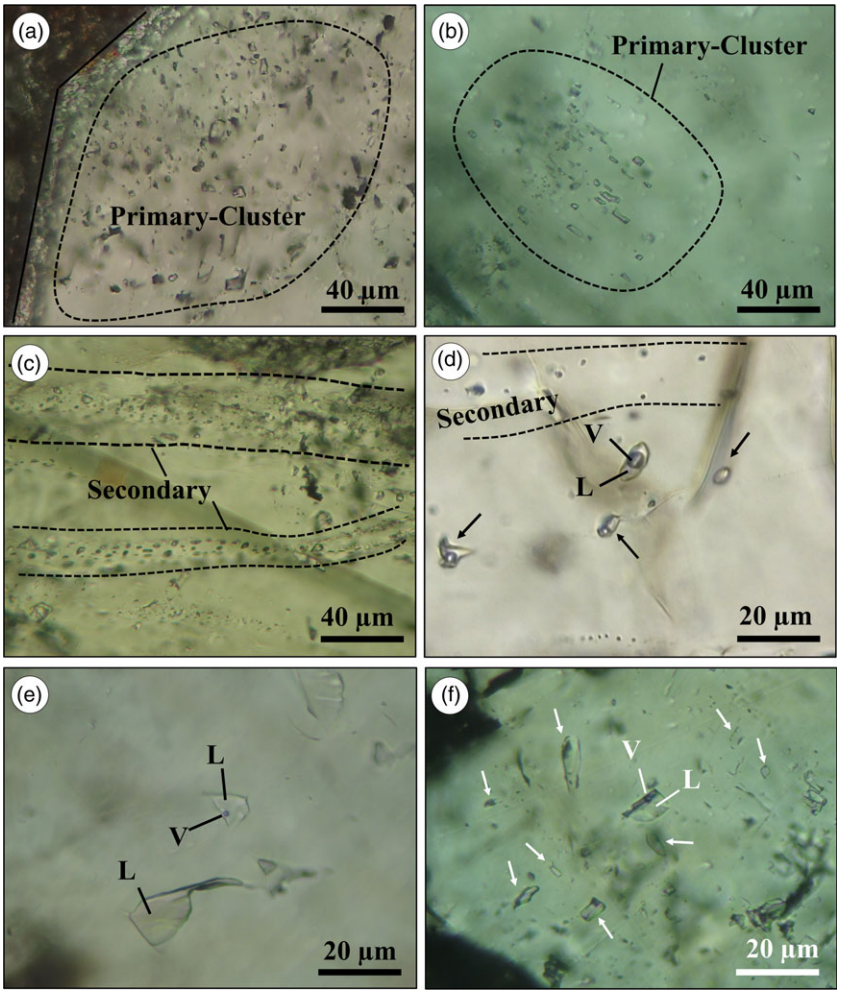

Figure 11. (Colour online) Fluid inclusions photomicrographs in the Chahmileh deposit. (a) Primary cluster of fluid inclusions relative to the quartz grain boundary, (b) Primary cluster of fluid inclusions hosted by calcite, (c) A row of secondary fluid inclusions in calcite, (d) Primary liquid-rich two-phase fluid inclusions with secondary fluid inclusions in quartz, (e) Association of liquid-rich two-phase (L+V) with liquid monophase (L) fluid inclusions hosted in quartz, (f) Primary liquid-rich two-phase fluid inclusions in dolomite.

211.0 °C (avg. = 173.9 °C, $n = 28$). The Tm_{ice} value for these inclusions varies from −16.8 to −12.2 °C (avg. = −14.2 °C, $n = 28$), corresponding to a salinity of 16.2–20.1 wt.% NaCl eq. (avg. = 17.9 wt.%, $n = 28$). Fluid density estimated for these fluid inclusions ranges from 0.96 to 1.06 g/cm^3.

The T_{fm} of primary liquid-rich fluid inclusions in quartz-galena veins from the main-ore stage III is in the range of −48.0 to −39.0 °C with an average of −42.1 °C, suggesting the presence of appreciable amount of $CaCl_2$, in addition to NaCl (Van den Kerkhof & Hein, 2001). Inclusions homogenized into the liquid phase between 147.0 and 198.0 °C (avg. = 171.1 °C, $n = 21$). Tm_{ice} values vary from −14.5 to −10.3 °C, with an average of −12.1 °C ($n = 21$), corresponding to a salinity of 14.3–18.2 wt.% NaCl eq. (avg. = 16.0 wt.%). Fluid density estimated for the fluid inclusions in these veins is in range of 0.97–1.07 g/cm^3.

The T_{fm} of primary liquid-rich fluid inclusions in late calcite veins of the post-ore stage is in range of −25.0 to −21.0 °C with an average of −22.6 °C. These values are close to the first ice-melting temperature of the NaCl–H_2O system (−20.8 °C), suggesting that NaCl is the principal salt in the solution. Inclusions homogenized into the liquid phase between 88.0 and 115.0 °C (avg. = 103.5 °C, $n = 12$). Tm_{ice} values for these inclusions vary from −9.3 to −5.6 °C with an average of −7.1 °C ($n = 12$), corresponding to a salinity of 8.7–13.2 wt.% NaCl eq. (avg. = 10.6 wt.%, $n = 12$). Fluid density estimated for the fluid inclusions in late calcite veins is in range of 0.88–0.95 g/cm^3.

5.3. Stable (C–O–S) isotopes

The $\delta^{13}C$ and $\delta^{18}O$ isotopic composition of eleven dolomite crystals (Dol-2), associated with the main-ore stage, is listed in Table 2 and shown in Fig. 14. Dolomite samples have $\delta^{13}C_{VPDB}$ and $\delta^{18}O_{VSMOW}$ values of −0.99 to +1.99‰ (avg. = +0.31‰) and +20.74 to +25.48‰ (avg. = +23.79‰), respectively. The $\delta^{13}C_{CO2}$ and $\delta^{18}O_{fluid}$ values for dolomite samples range from −0.89 to +2.09‰ and +11.04 to +15.78‰, respectively. The C–O isotope values are similar to those of carbonates in carbonate-hosted Pb-Zn deposits of the YAMB (Table 3), (S Maghfouri, unpub. PhD thesis, Univ. Tabriz, 2017; Maghfouri & Choulet, 2021), suggesting a similar source of carbon and oxygen.

Sulphur isotopic compositions of sulphides and baryte samples are presented in Table 4 and shown in Figs. 15, 16. The $\delta^{34}S_{VCDT}$ values of galena samples from the Chahmileh deposit show a narrow range between +6.3 and +8.2‰ with an average value of +7.2‰. The $\delta^{34}S_{VCDT}$ values of sphalerite and chalcopyrite range from +5.9 to +6.2‰ (avg. = +6.0‰, $n = 2$) and +1.4 to +3.4‰ (avg. = +2.6‰, $n = 3$), respectively. The $\delta^{34}S_{VCDT}$ values for baryte samples vary between +15.0 and +17.4‰ (avg. = +16.2‰, $n = 2$). The $\delta^{34}S$ values of equilibrated fluid were calculated using $\delta^{34}S$ value of sulphides and mineral-H_2S equilibrium isotopic fractionation factors (1000 lnα) based on Li and Liu (2006), assuming H_2S as the main sulphur species in the fluid (Table 4). Calculated $\delta^{34}S$ values of reduced sulphur (H_2S) in equilibrium with the

https://doi.org/10.1017/S0016756823000766 Published online by Cambridge University Press

Table 1. Microthermometric measurements of fluid inclusions from the Chahmileh deposit

Stages		Minerals (Sample no.)	Inclusion type	n	T_{fm} (°C)	Tm_{ice} (°C)	Th (°C)	Salinity (wt.% NaCl eq.)	Density (g/cm^3)
Main-ore stage	Stage I	Dol-2 (Tbm-5, B3-emaz-4,5)	LV (L)	4	−32 to −35	−13.4 to −15.1	133-186	17.3 to 18.7	1.02
				5	−32 to ?	−12.7 to −13.5	189-212	16.6 to 17.3	1.01
				5	−30 to −31	−13.3 to −15.2	177-216	17.2 to 18.8	1.04
				3	−29 to −33	−14.5 to −17.7	222-245	18.2 to 20.8	0.89
				3	nd	−12.3 to −14.5	203-225	16.2 to 18.2	0.95
				7	−30 to ?	−13.2 to −16.3	208-248	17.1 to 19.7	0.98
	Stage II	Qz-1 (T-wmaz-5)	LV (L)	5	−32 to −38	−12.3 to −15.8	136-152	16.2 to 19.3	0.96
				3	nd	−13.1 to −14.2	143-164	17.0 to 18.0	1.03
				7	−32 to −37	−14.6 to −15.3	166-180	18.3 to 18.9	1.02
				8	nd	−12.2 to −13.6	195-211	16.2 to 17.4	1.01
				5	−32 to −35	−14.5 to −16.8	187-205	18.2 to 20.1	1.06
	Stage III	Qz-2 (B3-emaz-2)	LV (L)	6	−41 to −44	−10.3 to −13.2	147-150	14.3 to 17.1	1.07
				4	−40 to −48	−11.7 to −13.5	157-178	15.7 to 17.3	0.98
				8	nd	−10.5 to −12.5	167-189	14.5 to 16.4	0.97
				3	−39 to −41	−11.1 to −14.5	188-198	15.1 to 18.2	0.99
Late veins		Cal-3 (T-wmaz-6)	LV (L)	2	−22 to −25	−7.5 to −9.3	88-103	11.1 to 13.2	0.88
				3	−21 to −22	−6.5 to −7.2	98-113	9.9 to 10.7	0.89
				4	−22 to −24	−5.6 to −7.3	101-115	8.7 to 10.9	0.93
				3	nd	−5.7 to −8.2	96-114	8.8 to 11.9	0.95

Abbreviations: Data are reported as averages of fluid inclusions assemblages; n = the number of available analyses, T_{fm} = first ice-melting temperature, Tm_{ice} = final ice-melting temperature, Th = homogenization temperature, LV = liquid-rich type, (L) = homogenization to liquid. nd = not detected.

sulphides range from a maximum of 11.0‰ in galena to a minimum of 1.2‰ in chalcopyrite.

5.4. Pb-isotope analyses

Lead isotopic compositions of galena samples from the Chahmileh deposit are presented in Table 5 and shown in Fig. 17. Galena samples ($n = 6$) have $^{206}Pb/^{204}Pb$ ratios ranging from 18.546 to 18.576, $^{207}Pb/^{204}Pb$ ratios ranging from 15.650 to 15.688 and $^{208}Pb/^{204}Pb$ ratios ranging from 38.795 to 38.918. $^{206}Pb/^{204}Pb$, $^{207}Pb/^{204}Pb$ and $^{208}Pb/^{204}Pb$ ratios for galena samples from the Pb–Zn deposits of the CIZ show the following ranges, respectively: 18.427 to 19.081, 15.586 to 15.722 and 38.500 to 38.910 (Table 5; Mirnejad *et al.* 2015), respectively. The Pb-isotope data of CIZ carbonate-hosted Pb–Zn deposits are similar to those obtained for the Chahmileh deposit, suggesting a similar lead source.

6. Discussion

6.1. Evolution of ore-forming fluids and ore controls

Carbonate-hosted Pb–Zn deposits are an important global source of Zn and Pb, which formed through fluid circulation within carbonate rocks (Leach *et al.* 2006, 2010a; Li *et al.* 2018). Temperature, salinity, pH and redox state (oxygen fugacity, fO_2) of fluids are crucial factors to control Zn and Pb mineralization (Cooke *et al.* 2000; Gómez-Fernández *et al.* 2000; Leach *et al.* 2001, 2005, 2010a; Conliffe *et al.* 2013).

The salinity-homogenization temperature diagram (Fig. 13a) of fluid inclusions shows a wide range of temperatures in dolomite and quartz samples (Th = 133.0–248.0 °C) and their salinities (14.3–20.8 wt.% NaCl eq.). Range of fluids salinities probably reflects mixing between high-temperature fluid (F_{ore}) (up to 248.0 °C) and high salinity (up to ~20.8 wt.% NaCl eq.) with a fluid (F_{sub}) characterized by high temperature and low salinity. These two fluids likely mixed at the site of sulphide deposition. Temperature and salinity of fluid inclusions at Chahmileh fall within the range of Irish-type and MVT Pb–Zn deposits (salinity = 10–35 wt.% NaCl eq. and temperature = 80–250 °C) and are typical of basinal brines (Wilkinson, 2001; Leach *et al.* 2005, 2010a). Relationship between homogenization temperature and salinity (Fig. 13b) indicates that basinal brine with some possible input from seawater fluid was responsible for ore mineralization at Chahmileh.

The ore precipitation mechanisms, common in numerous MVT and other sediment-hosted Pb-Zn ore deposits, include (i) cooling of hydrothermal fluid, (ii) pH decrease and (iii) mixing between two or more fluids (Anderson, 1973; Sverjensky, 1981). Upward migration of a metal-bearing, sulphur-depleted, hot brine (F_{ore}), originating from the Paleozoic basement, most likely mixed with a shallow, warm, metal-depleted, sulphur-rich reservoir (F_{sub}). Such mixing event accounts for the relatively wide range of salinity recorded in dolomite and quartz-hosted fluid inclusions.

Corbella *et al.* (2004), based on reactive transport modelling, demonstrated that fluid-mixing concomitantly triggers carbonate dissolution and precipitation of sulphides in MVT/sediment-hosted Pb–Zn deposits. The pH increases due to carbonate dissolution and a temperature decrease most likely contributed to the precipitation of the ore minerals. Such a fluid-mixing model

https://doi.org/10.1017/S0016756823000766 Published online by Cambridge University Press

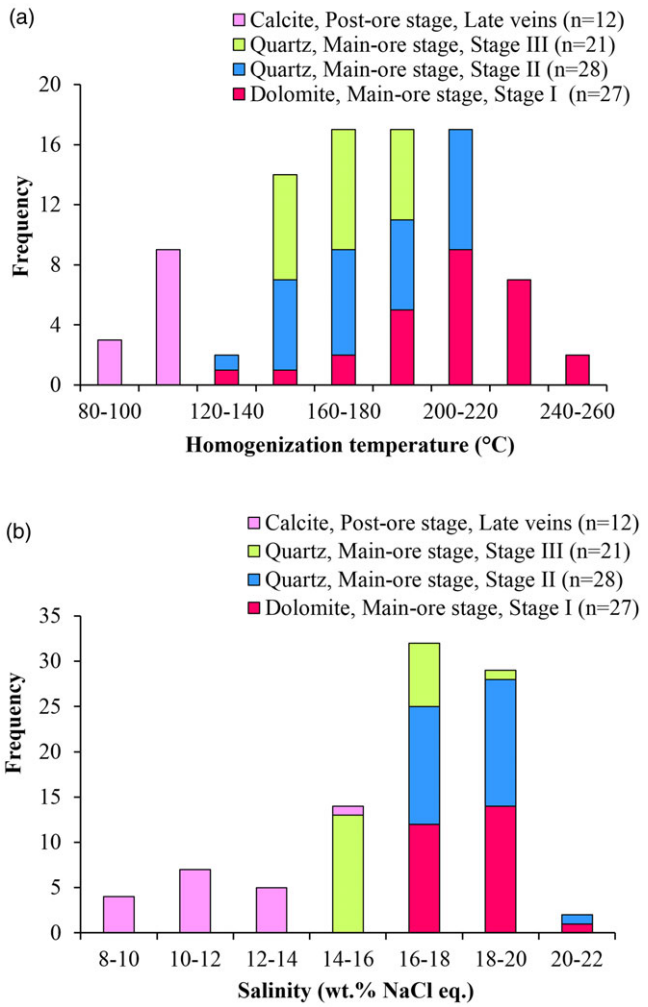

Figure 12. (Colour online) Histograms of total homogenization temperatures and calculated salinities based on microthermometric data of fluid inclusions from different mineralization stages.

has been proposed for numerous sediment-hosted Pb–Zn ore deposits where the mixing of a hot, metal-bearing fluid with a cooler, diluted fluid triggered ore precipitation (Beales & Jackson, 1966; Anderson, 1973; Sverjensky, 1986; Plumlee *et al.* 1994; Leach *et al.* 2005). In consideration of this evidence, it is likely that fluid dilution may have had an important role in ore deposition in the Chahmileh district (Fig. 13b).

Ore-forming hydrothermal fluids transport metals as ions and molecular complexes when migrating through the Earth's crust (Seward *et al.* 2014). Complexing with chloride and hydrosulphide/sulphide ligands is generally considered the important transport forms for silver, lead and zinc in the fluid systems, as demonstrated in some detail by several researchers (Seward, 1976; Ruaya & Seward, 1986; Sverjensky *et al.* 1997; Tagirov *et al.* 2007; Tagirov & Seward, 2010; Mei *et al.* 2015; Zhong *et al.* 2015). Metal complexing by chloride and bisulphide complexes is controlled by sulphide solubilities and the hydrothermal fluid temperature (Zhong *et al.* 2015). In low to medium temperature (< 350 °C) hydrothermal systems (MVT and SEDEX) (e.g., Chahmileh deposit), low sulphide solubilities dictate that the ore fluids cannot carry both reduced sulphur and metals. Hanor (1996) and Reed (2006) proposed that in ore-forming brines, transportation of Pb and Zn was mostly controlled by chloride complexes. Precipitation of sulphide minerals is probably a consequence of chloride complexe destabilization during fluid mixing and dilution. A chloride threshold of 100 $g.L^{-1}$ (salinity ~17 wt.% NaCl eq.) was calculated for metal transportation in the basinal brines (at temperatures of <150 °C) when the reduced sulphur concentrations were lower than 0.02 $mg.L^{-1}$ (Kharaka *et al.* 1987; Sicree & Barnes, 1996; Giordano, 2000). Therefore, it is reasonable to imply that concentration of chloride (110 $g.^{L-1}$) calculated based on fluid inclusion salinity data is enough to act as a complex for Pb and Zn migration. First ice-melting temperature measurements in fluid inclusions suggest the presence of Na^{+}, K^{+}, Ca^{+2} and Mg^{+2} as dissolved cations in the ore-forming fluid inclusions in the Chahmileh deposit. These cations were probably leached from the sedimentary units and transported as chloride complexes (Sverjensky, 1989) in the hydrothermal solution.

Possible processes that significantly invoked increasing the chlorine content of seawater trapped in the sediments include; shale membrane filtration (Graf, 1982; AMF Garavito Rojas, unpub. PhD thesis, Univ. Vrije, 2006), maturation of white mica (sericite and muscovite) (Michalik, 1997) and hydration of detrital clastic minerals (biotite) to sheet silicates (sericite or chlorite) via diagenesis (Gleeson *et al.* 2003). Identifying the exact mechanism for the source(s) of Cl in the Chahmileh deposit needs further scrutiny, but high chloride content of the metalliferous hydrothermal fluid in the Chahmileh deposit is inferred from fluid inclusion data.

6.2. Source of CO_2

There are three principal sources of carbon and oxygen in hydrothermal fluids: (I) mantle, (II) marine carbonate rocks and (III) sedimentary organic matter (Taylor *et al.* 1967; Veizer & Hoefs, 1976; Demény & Harangi, 1996; Liu & Liu, 1997; Demény *et al.* 1998). The $\delta^{13}C_{VPDB}$ and $\delta^{18}O_{VSMOW}$ values of the mantle, marine carbonate and organic matter range from −8.0 to −4.0‰, +6.0 to +10.0‰ (Taylor *et al.* 1967), −4.0 to +4.0‰ and +20.0 to +30.0‰ (Veizer & Hoefs, 1976) and −30.0 to −10.0‰ and +24.0 to +30.0‰ (Liu & Liu, 1997), respectively. The $\delta^{18}O_{VSMOW}$ values plotted against $\delta^{13}C_{VPDB}$ for dolomite samples of the main-ore stage are higher than typical values for igneous carbonate and somewhat lower than those of organic sediments, but are similar to those of marine carbonate rocks (Fig. 14). Thus, the carbon and oxygen isotopic data indicate that the CO_2 in the ore-forming fluid (hydrothermal dolomite) likely originated from the dissolution of marine carbonates. Therefore, the Triassic dolomitic marble of the Chah Gorbeh Complex was likely the main source of CO_2 in the ore-forming fluid. The CO_2 produced by dissolution of Triassic dolomitic marble will increase H_2CO_3 content and activity, making the fluid more acidic and dissolving further carbonates until it reaches chemical equilibrium with dolomitic marble (Spangenberg *et al.* 1996). We plotted both $\delta^{13}C_{VPDB}$ and $\delta^{18}O_{VSMOW}$ values of carbonate samples from Mediabad, Farahabad, Mansourabad and Darre Zanjr deposits in Fig. 14. The isotopic data plot near those of marine carbonates and/or between the marine carbonate and sedimentary organic matter field. Thus, the similarity in C-O isotope ratios for the Pb-Zn deposits located within YAMB suggests a similar source for CO_2 in the ore-forming fluids, which likely originated from dissolution of marine carbonate rocks or dihydroxylation of sedimentary organic matter during mineralization.

Calcite and dolomite are two main C-bearing hydrothermal minerals in the Chahmileh deposit. H_2CO_3 (present as CO_2

https://doi.org/10.1017/S0016756823000766 Published online by Cambridge University Press

Table 2. Carbon and oxygen isotopic composition of main-ore stage dolomite (Dol-2) at the Chahmileh deposit

Sample no.	$\delta^{13}C_{VPDB}$ (‰)	$\delta^{18}O_{VPDB}$ (‰)	$\delta^{18}O_{VSMOW}$ (‰)[a]	$\delta^{13}C_{CO2}$ (‰)[b]	$\delta^{18}O_{fluid}$(‰)[c]
Chahmileh −01	0.37	−5.66	25.07	0.47	15.37
Chahmileh −02	0.14	−5.26	25.48	0.24	15.78
Chahmileh −03	0.33	−6.45	24.26	0.43	14.56
Chahmileh −04	1.45	−7.39	23.29	1.55	13.59
Chahmileh −05	1.99	−8.18	22.47	2.09	12.77
Chahmileh −06	0.69	−6.95	23.74	0.79	14.04
Chahmileh −07	−0.64	−8.27	22.38	−0.54	12.68
Chahmileh −08	0.72	−5.94	24.78	0.82	15.08
Chahmileh −09	−0.51	−5.70	25.03	−0.41	15.33
Chahmileh −10	−0.09	−6.26	24.45	0.01	14.75
Chahmileh −11	−0.99	−9.86	20.74	−0.89	11.04

[a] $\delta^{18}O_{VSMOW} = 1.03091\ (\delta^{18}O_{VPDB}) + 30.91$ (Friedman and O'Neil 1977),
[b] $1000\ln\alpha_{(CO2\text{-}dolomite)} = -1.637\times 10^6/(T+273.15)^2 + 7.290$ (Horita 2014),
[c] $1000\ln\alpha_{(dolomite\text{-}fluid)} = 4.60\times 10^6/(T+273.15)^2 - 4.650\times 10^3/(T+273.15) + 1.710$ (Zheng 1999). $T = 205.3$ °C, based on microthermometry analysis of fluid inclusion in dolomite (Dol-2) from the main sulphide stage

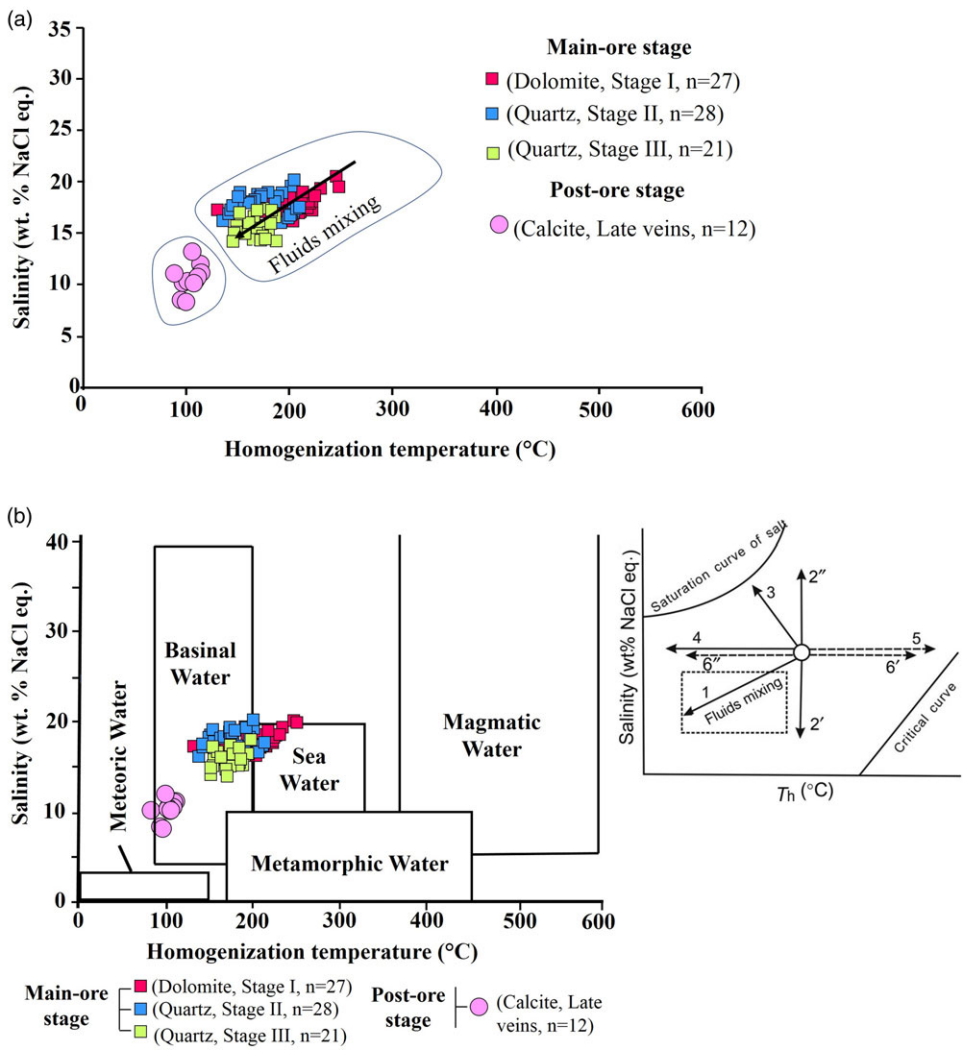

Figure 13. (Colour online) (a) Salinity versus homogenization temperature of fluid inclusions hosted in dolomite, quartz and calcite from the Chahmileh deposit, (b) Salinity versus total homogenization temperature and possible fluid composition of the Chahmileh deposit (Kesler, 2005). Fluid evolution trends are represented by arrows from Shepherd *et al.* (1985). Notes: trend 1 represents primitive fluid A mixed with cold and low salinity fluid B; trends 2 and 2' represent the result of fluid A isothermally mixing with different salinity fluid B; trend 3 represents the salinity of residual phase increased, caused by boiling of fluid A; trend 4 represents cooling of fluid A; trend 5 represents leakage of fluid inclusions during heating; and trend 6 represents necking down of the fluid inclusion.

https://doi.org/10.1017/S0016756823000766 Published online by Cambridge University Press

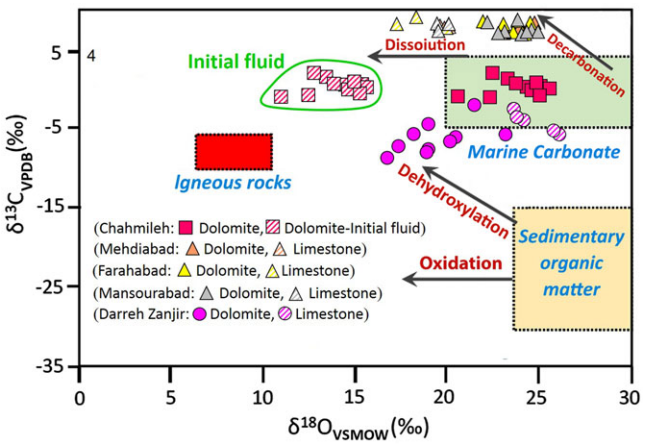

Figure 14. (Colour online) $\delta^{13}C_{VPDB}$ versus $\delta^{18}O_{VSMOW}$ diagram showing isotopic composition of dolomitic host rock of the Chahmileh deposit and isotopic composition of mineral separates from Mediabad, Farahabad, Mansourabad and Darre Zanjir deposits of YAMB. Given range by Taylor & McLennan (1985) and Hoefs (2015).

(aqueous)) and HCO_3^- are two key C-bearing species in hydrothermal fluids. Given that the C isotope fractionation between H_2CO_3 or HCO_3^- (aq.) and CO_2 (gas) is negligible, i.e., $\delta^{13}C_{fluid} \approx \delta^{13}C_{CO2}$ (Ohmoto, 1972), it is possible to estimate the theoretical $\delta^{13}C_{fluid}$ value from calculated value of $\delta^{13}C_{CO2}$. Assuming an average homogenization temperature of 205 °C (fluid inclusions in dolomite samples associated with the main-ore stage, Fig. 9), the $\delta^{13}C_{CO2}$ values are in the range of −0.89 to +2.09‰, calculated using the $1000\ln\alpha_{(CO2\text{-}dolomite)} = -1.637\times 10^6/(T+273.15)^2 + 7.290$ function (Horita, 2014; $T = 205.3$ °C). Similarly, $\delta^{18}O_{fluid}$ values vary from +11.04 to +15.78‰ and were calculated using the $1000\ln\alpha_{(dolomite\text{-}fluid)} = 4.60\times 10^6/(T+273.15)^2 - 4.650\times 10^3/(T+273.15) + 1.710$ function (Zheng 1999; $T = 205.3$ °C). The theoretical $\delta^{13}C_{CO2}$ and $\delta^{18}O_{fluid}$ values suggest that source of C is likely the ^{13}C-enriched marine carbonate, while O is possibly derived from a mixed source of ^{18}O-depleted metamorphic water and ^{18}O-enriched dolomitic marble.

6.3. Source of sulphur and mechanisms of sulphide deposition

Sulphur isotopic compositions of sulphur-bearing minerals are mostly affected by the source and fractionation processes (Ohmoto & Goldhaber, 1997; Seal *et al.* 2006; Hoefs, 2015). Sulphides in carbonate-hosted Pb-Zn deposits show wide ranges of $\delta^{34}S$ (Fig. 16a), with values from lower than −25‰ to higher than +35‰ (Leach *et al.* 2005). However, the Chahmileh Pb-Zn deposit sulphides show a relatively narrow range of $\delta^{34}S$ values, from +1.4 to +8.2‰, with an average of +5.4‰ (Figs. 15, 16). Although this narrow range may be caused by the limited number of analysed samples of sulphides, the $\delta^{34}S$ values also may suggest a uniform isotopic composition of the source and uniform conditions governing the isotopic fractionation between sulphur species in the ore-forming fluids during mineralization. The observed $\delta^{34}S_{PbS} > \delta^{34}S_{ZnS}$ trend suggests that ore minerals were precipitated under disequilibrium conditions, which are typical of ore formation at temperatures well below 250 °C (Ohmoto & Rye, 1979; Ohmoto, 1986).

The original fluid $\delta^{34}S_{H2S}$ can be estimated from $\delta^{34}S$ values of hydrothermal ore minerals. Under physical and chemical conditions (T < 300 °C, low pH, and Eh) envisaged for the main-stage fluids, the major sulphur species would be H_2S (Ohmoto & Rye, 1979). At these temperatures, sulphide dominance causes sulphide mineral $\delta^{34}S$ values to be close to the original fluid $\delta^{34}S_{H2S}$ (Ohmoto & Rye, 1979). The original fluid $\delta^{34}S_{H2S}$ values in equilibrium with sulphide minerals were estimated to be in range of +1.2‰ to +11.0‰ (avg. = +6.6‰).

Predominant source of sulphur in sediment-hosted Zn−Pb−(Cu−Ag−Ba) deposits is seawater sulphate (Leach *et al.* 2005, 2010a; Magnall *et al.* 2016), and sulphur isotopic composition of the Triassic seawater suphate ranges from +11‰ to +20‰ (Fig. 16b) (Claypool *et al.* 1980; Bottrell & Newton, 2006). The Triassic age of carbonates hosting the Chahmileh deposit and the $\delta^{34}S$ values for baryte (+15.0‰ and +17.4‰) (Fig. 16b) fall in the range of Triassic marine sulphate. Sulphide can be produced from seawater sulphate either by biogenic processes (bacterial sulphate reduction, BSR) or abiogenically via thermochemical processes (thermochemical sulphate reduction, TSR) (Machel, 2001). Values of $\delta^{34}S$ are also dependent on other factors, such as the sulphate reduction rate (Leavitt *et al.* 2013), sulphate concentration (Habicht *et al.* 2002), temperature (Sawicka *et al.* 2012), content of organic-rich matter in sediments (Goldhaber *et al.* 1995) and rate of sulphate replacement by sulphides (Rajabi *et al.* 2020). BSR usually takes place at 60–80 °C (Machel, 1989), although its occurrence at 110 °C has also been reported (Jørgenson *et al.* 1992). BSR commonly produces a wide $\delta^{34}S_{VCDT}$ range due to the large isotopic fractionation (15–66‰) between sulphate and sulphide (Rees, 1973; Leach *et al.* 2005; Basuki *et al.* 2008; Sim *et al.* 2011; Li *et al.* 2019). In contrast, TSR (occur at 150–350 °C) produces a relatively narrow range for sulphur isotopic fractionation, yielding <15‰ in the presence of organic matter (Ohmoto, 1972; Ohmoto & Rye 1979; Worden *et al.* 1995; Wang *et al.* 2018). Moreover, mixing of hot and cold ore-forming fluids could form S^{2-} from SO_4^{2-} by TSR through the $SO_4^{2-} + 2C = S^{2-} + 2CO_2$, $SO_4^{2-} + CH_4 = H_2S + CO_3^{2-} + H_2O$, or $SO_4^{2-} + 2CH_2O = H_2S + 2HCO^3$-reaction (Worden *et al.* 1995; Leach *et al.* 2005). TSR has been invoked as an important sulphate reduction process in MVT deposits (Leach *et al.* 2005; Wilkinson, 2014). In the Chahmileh deposit, the narrow range of positive $\delta^{34}S$ values of the sulphide minerals (+1.4 to +8.2‰) suggests that sulphur was probably supplied by the TSR process since Th values during ore formation at the Chahmileh (133.0 °C to 248.0 °C) are unfavourable for BSR (Kyle & Saunders, 1996; Leach *et al.* 2005).

6.4. Source of metals

The Pb isotopic compositions of galena in Chahmileh Pb-Zn deposit are quite homogeneous, which implies that Pb was supplied from either a completely homogenized mixed source or a single source. On a thorogenic diagram, Pb compositions show a positive linear correlation between the lower and upper crust curves, reflecting a likely mixing between multiple endmembers while the uranogenic isotope diagram shows more complexity. Data plot between the orogen and upper crust growth curves, suggesting a possible heterogeneous source for Pb (Fig. 17). These variations likely reflect a contribution from different crustal sources to the Pb mineralization. Crustal sources of Pb are also reflected by higher U/Pb ratios and high $^{206}Pb/^{204}Pb$ ratios, as revealed by calculated μ values (Zartman & Doe, 1981). Since Pb-isotope data of possible source rocks in the region are not available, the ultimate source(s) of Pb is unclear. However, like other Pb-Zn deposits in the CIZ (Fig. 17), the source(s) of Pb were likely continental crust or pelagic sediments developed during orogenic

https://doi.org/10.1017/S0016756823000766 Published online by Cambridge University Press

Table 3. Carbon and oxygen isotopic composition of mineral separates from the Pb–Zn deposits of Yazd-Anarak Metallogenic Belt

Sample no.	Minerals	$\delta^{13}C_{VPDB}$ (‰)	$\delta^{18}O_{VSMOW}$ (‰)	Sample no.	Minerals	$\delta^{13}C_{VPDB}$ (‰)	$\delta^{18}O_{VSMOW}$ (‰)
Mehdiabad-01[a]	Dolomite	2.9	24.3	Mansourabad-04[a]	Dolomite	2.7	23.2
Mehdiabad-02[a]	Dolomite	2.6	23.9	Mansourabad-05[a]	Dolomite	2.0	23.8
Mehdiabad-03[a]	Dolomite	2.8	23.2	Mansourabad-06[a]	Dolomite	2.3	22.3
Mehdiabad-04[a]	Dolomite	2.1	24.7	Mansourabad-07[a]	Dolomite	2.9	24.9
Mehdiabad-05[a]	Dolomite	2.2	24.5	Mansourabad-08[a]	Dolomite	3.3	23.9
Mehdiabad-06[a]	Dolomite	3.1	23.1	Mansourabad-09[a]	Limestone	2.2	19.7
Mehdiabad-07[a]	Dolomite	2.5	24.6	Mansourabad-10[a]	Limestone	2.5	20.3
Mehdiabad-08[a]	Limestone	2.4	20.4	Mansourabad-11[a]	Limestone	2.7	19.8
Mehdiabad-09[a]	Limestone	2.3	19.8	Darreh-Zanjir-01[b]	Dolomite	−2.2	21.5
Mehdiabad-10[a]	Limestone	2.6	20.0	Darreh-Zanjir-02[b]	Dolomite	−9.3	16.9
Farahabad-01[a]	Dolomite	2.2	23.1	Darreh-Zanjir-03[b]	Dolomite	−6.5	18.1
Farahabad-02[a]	Dolomite	2.1	22.0	Darreh-Zanjir-04[b]	Dolomite	−8.4	19.1
Farahabad-03[a]	Dolomite	3.2	24.2	Darreh-Zanjir-05[b]	Dolomite	−7.6	20.1
Farahabad-04[a]	Dolomite	2.4	24.5	Darreh-Zanjir-06[b]	Dolomite	−4.4	19.6
Farahabad-05[a]	Dolomite	2.9	23.5	Darreh-Zanjir-07[b]	Dolomite	−7.1	17.1
Farahabad-06[a]	Dolomite	3.1	24.1	Darreh-Zanjir-08[b]	Dolomite	−5.9	23.3
Farahabad-07[a]	Dolomite	2.1	23.8	Darreh-Zanjir-09[b]	Dolomite	−6.8	20.5
Farahabad-08[a]	Limestone	1.9	18.4	Darreh-Zanjir-10[b]	Dolomite	−8.2	19.6
Farahabad-09[a]	Limestone	2.6	20.2	Darreh-Zanjir-11[b]	Limestone	−2.5	23.5
Mansourabad-01[a]	Limestone	2.5	17.3	Darreh-Zanjir-12[b]	Limestone	−6.5	26.1
Mansourabad-02[a]	Dolomite	2.9	24.3	Darreh-Zanjir-13[b]	Limestone	−3.5	24.1
Mansourabad-03[a]	Dolomite	2.6	24.5	Darreh-Zanjir-14[b]	Limestone	−3.14	23.8

[a]Maghfouri (2017).
[b]Maghfouri & Choulet (2021).

Table 4. Sulphur isotopic composition of sulphide minerals and barytes from the Chahmileh deposit

Sample no.	Mineralization stages	Minerals	$\delta^{34}S_{VCDT}$ (‰)	Th (°C) (fluid calculated)	1000 lnα (Li & Liu 2006)	$\delta^{34}S_{H2S}$ (‰)
Tbm-8	Main-ore stage, stage III	Galena	8.2	205.3	−2.8	11.0
B1emaz-5	Main-ore stage, stage II	Galena	6.9	173.9	−3.2	10.1
B2emaz-3	Main-ore stage, stage II	Galena	6.3	173.9	−3.2	9.5
Twmaz-2	Main-ore stage, stage I	Galena	7.6	171.1	−3.2	10.8
B2emaz-3	Main-ore stage, stage III	Sphalerite	6.2	171.1	0.5	5.7
B2emaz-3	Main-ore stage, stage II	Sphalerite	5.9	171.1	0.5	5.4
Tremaz-11	Main-ore stage, stage I	Chalcopyrite	1.4	205.3	0.2	1.2
Dm-7	Main-ore stage, stage I	Chalcopyrite	3.4	205.3	0.2	3.2
Tbm-8	Main-ore stage, stage I	Chalcopyrite	3.2	205.3	0.2	3.0
Tbm-4	Post-ore stage, late gangue	Baryte	15.0	–	–	–
Tbm-4	Post-ore stage, late gangue	Baryte	17.4	–	–	–

activities (Mirnejad *et al.* 2015). In Pb–Zn deposits of the CIZ and Alborz Zone (AZ), most of the galena yield Pb model 'ages' of ~140 and ~250 Ma, indicating that mineralization resulted from the extraction of ore-bearing fluids from Upper Triassic–Lower Jurassic sequences (Mirnejad *et al.* 2015). The similarity in Pb-isotope ratios for the Pb-Zn deposits located within these zones suggests similar crustal evolution histories. Mirnejad *et al.* (2015) argued that Pb-Zn mineralization in sedimentary and igneous

https://doi.org/10.1017/S0016756823000766 Published online by Cambridge University Press

Table 5. The Pb isotopic composition of galena samples from the Chahmileh deposit and Pb–Zn deposits of the Central Iran Zone

Sample no.		$^{206}Pb/^{204}Pb$ (2σ)	$^{207}Pb/^{204}Pb$ (2σ)	$^{208}Pb/^{204}Pb$ (2σ)
CIZ	Chahmileh-01[a]	18.576 ± 0.120	15.688 ± 0.180	38.918 ± 0.24
	Chahmileh-02[a]	18.572 ± 0.120	15.685 ± 0.180	38.908 ± 0.24
	Chahmileh-03[a]	18.546 ± 0.120	15.650 ± 0.180	38.795 ± 0.24
	Chahmileh-04[a]	18.563 ± 0.120	15.665 ± 0.180	38.838 ± 0.24
	Chahmileh-05[a]	18.572 ± 0.120	15.667 ± 0.180	38.846 ± 0.24
	Chahmileh-06[a]	18.569 ± 0.120	15.658 ± 0.180	38.814 ± 0.24
	Qullehkaftaran[b]	18.461 ± 0.004	15.586 ± 0.004	38.500 ± 0.011
	Nakhlak[b]	18.516 ± 0.002	15.638 ± 0.002	38.641 ± 0.006
	Nakhlak[b]	18.511 ± 0.005	15.637 ± 0.005	38.642 ± 0.013
	Chahsorb[b]	18.427 ± 0.004	15.647 ± 0.004	38.575 ± 0.012
	Kamarmehdi[b]	19.081 ± 0.003	15.722 ± 0.003	38.910 ± 0.009
	Geijerkuh[b]	18.514 ± 0.003	15.704 ± 0.004	38.696 ± 0.013
	Mehdiabad[b]	18.499 ± 0.003	15.658 ± 0.003	38.634 ± 0.010

[a]This study.
[b]Mirnejad *et al.* (2015).

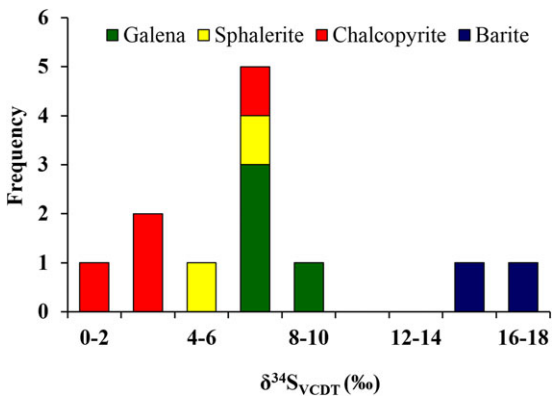

Figure 15. (Colour online) Histogram of sulphur isotopic compositions of various sulphides and sulphate minerals of the Chahmileh deposit.

rocks of the CIZ and AZ tectonic regions occurred following the Late Cretaceous-Tertiary accretionary stage of crustal thickening.

Different types of Pb-Zn deposits have different Pb isotopic signatures (Sangster *et al.* 2000), though the great majority of MVT deposits have $^{206}Pb/^{204}Pb$ values of 17.5–23 and $^{207}Pb/^{204}Pb$ values of 15.4–16.2 (Leach *et al.* 2005). The Pb isotopic composition of galena samples from Chahmileh also falls in this broad range (average $^{206}Pb/^{204}Pb = 18.566$ and $^{207}Pb/^{204}Pb = 15.668$). The Pb-isotope data suggest an orogenic reservoir coupled with a large contribution from crustal basement rocks as metal sources for the Chahmileh deposits; a pattern reported for most MVT deposits (Leach *et al.* 2005).

6.5. Proposed genetic model

Three distinct categories of sediment-hosted Pb–Zn deposits have been proposed by Leach *et al.* (2005), DL Leach *et al.*, report (2010b) and Wilkinson (2014) based on their tectonic setting, host-rock sequence and geochemical characteristics: MVT-type, SEDEX-type and Irish-type. The Pb–Zn mineralization in the Chahmileh deposit is hosted by the Middle Triassic dolomitic marble of the Chah Gorbeh Complex. Due to the association of mineralization with carbonate rocks, this deposit is comparable to MVT- and Irish-type deposits. The Chahmileh deposit does not share many of the main features of the Irish-type deposits, as outlined by Leach *et al.* (2005) and Wilkinson (2014). Although it is hosted by carbonate rocks and shows open-space filling textures, mineralization is not a sub-seafloor replacement associated with synsedimentary normal faults, it did not form during diagenesis and the sulphides in the deposit do not show any synsedimentary textures. Instead, the Chahmileh Pb–Zn deposit has many features that match closely with those of most MVT deposits (Sangster, 1990; Leach *et al.* 2005). These features include: (1) the ore mineralization is epigenetic and stratabound; (2) there is no relationship between mineralization and igneous activity; (3) thrust and normal faults are indicative of a compression and extension geodynamic setting; (4) ore is mineralogically simple and composed dominantly of galena, sphalerite, pyrite, chalcopyrite and dolomite, quartz and calcite; (5) ore bodies show open-space filling, brecciated and replacement textures; (6) lack of exhalative processes or laminated ores; (7) hydrothermal alteration mainly consists of dolomitization and silicification, associated with host-rock dissolution and brecciation; (8) moderate to high Th values up to 248 °C, reflects the relatively high temperatures of ore formation that are not typical of many MVT deposits; (9) C-O isotopes suggest that CO_2 is originated from carbonate host rock; (10) the average $\delta^{34}S$ value of sulphide is lighter than contemporaneous seawater and (11) Pb isotopic data indicate crustal sources for the metals. Most of these evidences indicate that the Chahmileh deposit is similar to a typical MVT deposit (e.g., Leach *et al.* 2001, 2005, 2010b; Pirajno, 2009, 2013; Wilkinson, 2014) (Table 6).

Rajabi *et al.* (2012, 2013) proposed that the main Cimmerian (Upper Triassic) and Laramide (Late Cretaceous-Tertiary) orogenic collisions led to development of discordant, stratabound MVT deposits in different Pb–Zn metallogenic belts of Iran adjacent to the Paleo-Tethys and Neo-Tethys suture zones. The main Cimmerian orogenic event transformed the northern margin of the Iranian Plateau into a collisional foreland basin (Wilmsen *et al.* 2009). This compression 'squeezed' fluid from the foreland basin towards the Triassic carbonate platforms, and brines migrated in basin large-scale regional faults and fissures in the basement and overlying strata, extracted metals (i.e., Pb and Zn) and finally migrated to suitable host rocks (Chah Gorbeh Complex). Simultaneously, extensive hydrothermal fluid flow and circulation of reduced sulphur of sulphate in the overlying strata into thiosulphuric acid and hydrogen sulphuric acid migrated with the infiltrating fluid, eventually mixed with the reduced sulphur generated by pyrolysis of sulphur-containing organic matter in the wall rock. Once metal-bearing and reduced sulphur-bearing fluids mixed in favourable fracture zone(s), by changes in ore-forming conditions, metal sulphides precipitated and formed the ore bodies.

7. Summary and conclusions

The Chahmileh Pb–Zn deposit is a fault-controlled deposit located in the YAMB of the CIZ. It is composed of sulphide and non-sulphide ores hosted in Middle Triassic dolomitic marble of the

https://doi.org/10.1017/S0016756823000766 Published online by Cambridge University Press

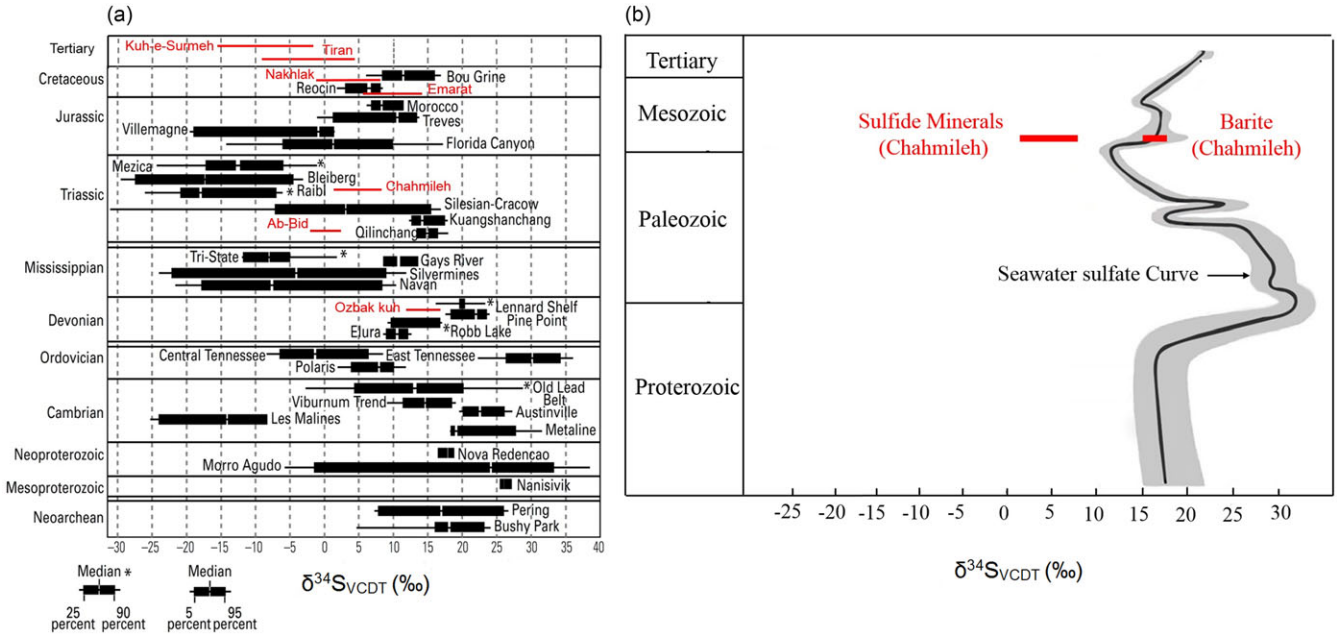

Figure 16. (Colour online) (a) $\delta^{34}S_{VCDT}$ values in sulphides of the Chahmileh deposit in comparison with range and median $\delta^{34}S$ values of sulphides in a selection of orogenic-related MVT deposits (data from Leach *et al.* 2010b; Ehya *et al.* 2010; Ehya, 2014; Jazi *et al.* 2017; Nejadhadad *et al.* 2018; Fazli *et al.* 2019; Rajabi *et al.* 2022), (b) Distribution of $\delta^{34}S$ values of baryte and sulphide minerals from the Chahmileh deposit in relation to age curve for sulphur (Claypool *et al.* 1980; Bottrell & Newton, 2006).

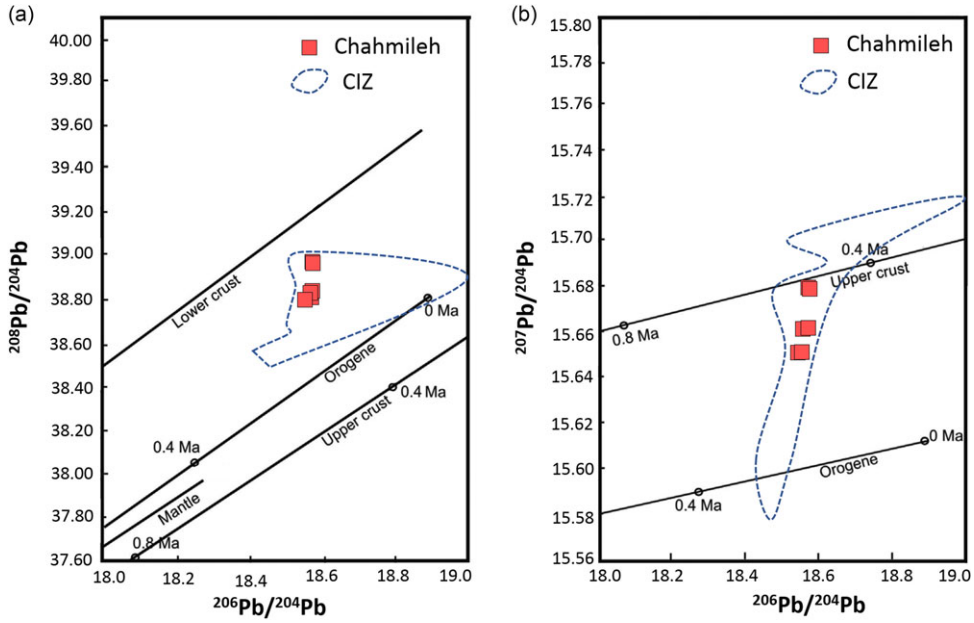

Figure 17. (Colour online) (a) and (b) Pb isotopic ratios of galena samples on a 'plumbo-tectonic' diagram (Zartman & Doe, 1981). The Pb-isotope data of galena from the Central Iran Zone (Mirnejad *et al.* 2015) are presented for comparison.

Chah Gorbeh Complex. The main sulphides are galena, sphalerite and minor amounts of chalcopyrite and pyrite, which were partially or completely transformed into non-sulphide minerals by supergene processes. Cerussite, hemimorphite, wulfenite, malachite, mimetite, smithsonite and iron oxy-hydroxides are the main non-sulphide ore minerals. Fluid mixing and dilution is the most probable mechanism of ore-forming fluids evolution. Carbon and oxygen isotopic compositions of dolomite suggest that CO_2 in the ore-forming hydrothermal fluids mainly originated from marine carbonate rocks. TSR is the most likely process of supplying reduced sulphur for sulphide deposition. Pb in the deposit originated from an orogenic source, which was dominated by upper crustal rocks with high $^{238}U/^{204}Pb$ and $^{232}Th/^{204}Pb$ ratios. Ore precipitation is mostly initiated by interaction of the ore-bearing fluid with carbonate host rocks, accompanied by decreasing temperature, increasing pH and perhaps a drop-in oxygen fugacity, and therefore, with a concomitant increase in the reduced sulphur content by a TSR mechanism. The Chahmileh deposit system is likely an MVT-type Pb–Zn deposit, related to the thrust compression-driven fluid flow, developed in Middle Triassic carbonate strata.

https://doi.org/10.1017/S0016756823000766 Published online by Cambridge University Press

Table 6. Comparison between MVT deposits and the Chahmileh Pb–Zn deposit

Characteristics	MVT deposits	Chahmileh Pb–Zn deposit
Grades (Pb+Zn)	avg. < 10 wt.%	avg. 2.15 wt.%
Host rocks	Cambrian to Late Carboniferous and Triassic to Cretaceous dolostone and limestone	Middle Triassic dolomitic marble
Mineralization style	Epigenetic	Epigenetic
Ore body morphology	Stratabound and concordant with fault	Stratabound and concordant with normal fault
Relation with magmatic activity	Absence of temporally or spatial association with igneous activities	No evidence of magmatic activation in the ore-bearing sequence
Mineral compositions	Sphalerite, galena, pyrite, baryte, fluorite, dolomite and calcite	Galena, sphalerite, chalcopyrite, pyrite, quartz, dolomite, calcite and baryte
Ore textures and structures	Vein-veinlet, replacement and open-space karst filling	Vein-veinlet, open space, breccia and replacement
Ore-controlled factors Mainly	Mainly controlled by open structure and lithology	Mainly controlled by normal fault and dolomitic marble host rock
Alteration	Dolomitization, host-rock dissolution and brecciation	Dolomitization, silicification, host-rock dissolution and brecciation
Main ore metals	Pb–Zn	Pb–Zn
Fluid inclusions	Salinity: 10–30 wt.% NaCl eq. Th: 50–200 °C	Salinity: 14.3–20.8 wt.% NaCl eq. Th: 133.0–248.0 °C
C–O isotopes	Sourced from carbonate rocks	Sourced from carbonate rocks
S isotope	+10 to +25‰, sourced from seawater sulphate	+1.4 to +8.2‰, sourced from seawater sulphate
Pb isotope	Soured from basement	Soured from basement
References	Leach *et al.* (2005, 2010b), Wilkinson (2014)	This paper

Acknowledgements. This paper is part of the second author's PhD research thesis, supported by partial grant from the Kharazmi University (Iran). The authors acknowledge financial support from the Iranian Mines and Mineral Industries Development and Renovation Organization. We would like to thank Dr. J.H. Curtis from the Stable Isotope Mass Spectroscopy Laboratory, University of Florida, for his assistance in carbon-oxygen isotope analysis, and Dr. D. Dettman from the Environmental Isotope Laboratory at the University of Arizona for his help in sulphur isotope analysis. Author would like to thank Prof. Paul Spry for his thorough review, constructive comments and massive improvement of the manuscript.

References

Alavi M (1991) *Tectonic map of the Middle East, Scale 1:5,000,000*. Tehran: Geological Survey of Iran.

Anderson GM (1973) The hydrothermal transport and deposition of galena and sphalerite near 100 degrees C. *Economic Geology* **68**, 480–92. https://doi.org/10.2113/gsecongeo.68.4.480

Bagheri S and Stampfli GM (2008) The Anarak, Jandaq and Posht-e-Badam metamorphic complexes in Central Iran: new geological data, relationships and tectonic implications. *Tectonophysics* **451**, 123–55. https://doi.org/10.1016/j.tecto.2007.11.047

Balini M, Nicora A, Berra F, Garzanti E, Levera M, Mattei M, Muttoni G, Zanchi A, Bollati I, Larghi C, Zanchetta S, Salamati R and Mossavvari F (2009) The Triassic stratigraphic succession of Nakhlak (Central Iran), a record from an active margin. In *South Caspian to Central Iran Basins* (eds MF Brunet, JW Granath and M Wilmsen), pp. 287–321. Geological Society of London, Special Publications no. 312.

Basuki NI, Taylor BE and Spooner ETC (2008) Sulfur isotope evidence for thermochemical reduction of dissolved sulfate in Mississippi Valley-type zinc-lead mineralization, Bongara area, Northern Peru. *Economic Geology* **103**, 783–99. https://doi.org/10.2113/gsecongeo.103.4.783

Beales FW and Jackson SA (1966) Precipitation of lead-zinc ores in carbonate reservoirs as illustrated by Pine Point ore field, Canada. *Transactions of the Institution of Mining and Metallurgy* **75**, B278–85.

Berberian M (1981) Active faulting and tectonics of Iran. In *Zagros-Hindu Kush Himalaya Geodynamic Evolution* (eds HK Gupta and FM Delany), pp. 33–69. American Geophysical Union, *Geodynamic Series* 3.

Berra F, Zanchi A, Angiolini L, Vachard D, Vezzoli G, Zanchetta S, Bergomi M, Javadi HR and Kouhpeyma M (2017) The upper Palaeozoic Godar-e-Siah Complex of Jandaq: evidence and significance of a North Palaeotethyan succession in Central Iran. *Journal of Asian Earth Sciences* **138**, 272–90. https://doi.org/10.1016/j.jseaes.2017.02.006

Bodnar RJ (1993) Revised equation and table for determining the freezing point depression of H_2O-NaCl solutions. *Geochimica et Cosmochimica Acta* **57**, 683–84. https://doi.org/10.1016/0016-7037(93)90378-A

Bottrell SH and Newton RJ (2006) Reconstruction of changes in global sulfur cycling from marine sulfate isotopes. *Earth-Science Reviews* **75**, 59–83. https://doi.org/10.1016/j.earscirev.2005.10.004

Brown PE (1989) FLINCOR; a microcomputer program for the reduction and investigation of fluid-inclusion data. *American Mineralogist* **74**, 1390–93.

Buchs DM, Bagheri S, Martin L, Hermann J and Arculus R (2013) Palaeozoic to Triassic ocean opening and closure preserved in Central Iran: constraints from the geochemistry of meta-igneous rocks of the Anarak area. *Lithos* **172-173**, 267–87. https://doi.org/10.1016/j.lithos.2013.02.009

Claypool GE, Holser WT, Kaplan IR, Sakai H and Zak I (1980) The age curves of sulfur and oxygen isotopes in marine sulfate and their mutual interpretation. *Chemical Geology* **28**, 199–260. https://doi.org/10.1016/0009-2541(80)90047-9

Conliffe J, Wilton DHC, Blamey NJF and Archibald SM (2013) Paleoproterozoic Mississippi Valley type Pb-Zn mineralization in the Ramah Group, Northern Labrador: stable isotope, fluid inclusion and quantitative fluid inclusion gas analyses. *Chemical Geology* **362**, 211–23. https://doi.org/10.1016/j.chemgeo.2013.08.032

Cooke DR, Bull SW, Large RR and McGoldrick PJ (2000) The importance of oxidized brines for the formation of Australian Proterozoic stratiform sediment-hosted Pb-Zn (sedex) deposits. *Economic Geology* **95**, 1–18. https://doi.org/10.2113/gsecongeo.95.1.1

Corbella M, Ayora C and Cardellach E (2004) Hydrothermal mixing, carbonate dissolution and sulfide precipitation in Mississippi Valley-type deposits. *Mineralium Deposita* **39**, 344–57. https://doi.org/10.1007/s00126-004-0412-5

Corfu F (2004) U-Pb age, setting and tectonic significance of the anorthosite-mangerite-charnockite-granite suite, Lofoten-Vesteralen, Norway. *Journal of Petrology* **45**, 1799–819. https://doi.org/10.1093/petrology/egh034

Demény A, Ahijado A, Casillas R and Vennemann TW (1998) Crustal contamination and fluid/rock interaction in the carbonatites of Fuerteventura (Canary Islands, Spain): a C, O, H isotope study. *Lithos* **44**, 101–15. https://doi.org/10.1016/S0024-4937(98)00050-4

Demény A and Harangi SZ (1996) Stable isotope studies and processes of carbonate formation in Hungarian alkali basalts and lamprophyres: evolution of magmatic fluids and magma-sediment interactions. *Lithos* **37**, 335–49. https://doi.org/10.1016/0024-4937(95)00029-1

Diamond LW (2003) Introduction to gas-bearing, aqueous fluid inclusions. In *Fluid Inclusions: Analysis and Interpretation* (eds I Samson, A Anderson and D Marshall), pp. 101–58. Mineralogical Association of Canada, *Short Course Series* 32.

Ehya F (2014) The Paleozoic Ozbak-Kuh carbonate-hosted Pb-Zn deposit of East Central Iran: isotope (C, O, S, Pb) geochemistry and ore genesis. *Mineralogy and Petrology* **108**, 123–36. https://doi.org/10.1007/s00710-013-0279-1

Ehya F, Lotfi M and Rasa I (2010) Emarat carbonate-hosted Zn-Pb deposit, Markazi Province, Iran: a geological, mineralogical and isotopic (S, Pb) study. *Journal of Asian Earth Sciences* **37**, 186–94. https://doi.org/10.1016/j.jseaes.2009.08.007

Farbod Y, Bellier O, Shabanian E and Abbassi MR (2011) Geomorphic and structural variations along the Doruneh Fault System (Central Iran). *Tectonics* **30**, TC6014. https://doi.org/10.1029/2011TC002889

Fazli S, Taghipour B, Moore F and Lentz DR (2019) Fluid inclusions, S isotopes, and Pb isotopes characteristics of the Kuh-e-Surmeh carbonate-hosted Zn-Pb deposit in the Zagros Fold Belt, southwest Iran: implications for the source of metals and sulfur and MVT genetic model. *Ore Geology Reviews* **109**, 615–29. https://doi.org/10.1016/j.oregeorev.2019.04.006

Ghasemi A and Talbot CJ (2006) A new tectonic scenario for the Sanandaj-Sirjan Zone (Iran). *Journal of Asian Earth Sciences* **26**, 683–93. https://doi.org/10.1016/j.jseaes.2005.01.003

Giordano TH (2000) Organic matter as a transport agent in ore-forming systems. *Reviews in Economic Geology* **9**, 133–55. https://doi.org/10.5382/Rev.09.07

Gleeson SA, Yardley BWD, Munz IA and Boyce AJ (2003) Infiltration of basinal fluids into high-grade basement, South Norway: sources and behaviour of waters and brines. *Geofluids* **3**, 33–48. https://doi.org/1468-8123.2003.00047.x

Goldhaber MB and Orr WL (1995) Kinetic controls on thermochemical sulfate reduction as a source of sedimentary H2S. In *Geochemical Transformations of Sedimentary Sulfur* (eds MA Vairavamurthy and MAA Schoonen), pp. 412–25. *ACS Symposium Series* 612.

Gómez-Fernández F, Both RA, Mangas J and Arribas A (2000) Metallogenesis of Zn-Pb carbonate-hosted mineralization in the southeastern region of the Picos de Europa (Central Northern Spain) Province: geologic, fluid inclusion, and stable isotope studies. *Economic Geology* **95**, 19–40.

Graf DL (1982) Chemical osmosis, reverse chemical osmosis and the origin of subsurface brines. *Geochimica et Cosmochimica Acta* **46**, 1438–41. https://doi.org/10.1016/0016-7037(82)90277-0

Graton LC and Harcourt GA (1935) Spectrographic evidence on origin of ores of Mississippi Valley type. *Economic Geology* **30**, 800–24. https://doi.org/10.2113/gsecongeo.30.7.800

Habicht KS, Gade M, Thamdrup B, Berg P and Canfield DE (2002) Calibration of sulfate levels in the Archean ocean. *Science* **298**, 2372–74. https://doi.org/10.1126/science.1078265

Hanor JS (1996) Controls on the solubilization of Lead and Zinc in basinal brines. In *Carbonate-Hosted Lead-Zinc Deposits* (ed DF Sangster), pp. 483–500. Geological Society of London, Special Publication no. 4.

Hoefs J (2015) *Stable Isotope Geochemistry*, 7rd edn. Berlin: Springer-Verlag, 389 pp.

Horita J (2014) Oxygen and carbon isotope fractionation in the system dolomite-water-CO_2 to elevated temperatures. *Geochimica et Cosmochimica Acta* **129**, 111–24. https://doi.org/10.1016/j.gca.2013.12.027

Hou Z and Zhang H (2015) Geodynamics and metallogeny of the eastern Tethyan metallogenic domain. *Ore Geology Reviews* **70**, 346–84. https://doi.org/10.1016/j.oregeorev.2014.10.026

Javadi HM, Esterabi Ashtiani M, Guest B, Yassaghi A, Ghassemi MR, Shahpasandzadeh M and Naeimi A (2015) Tectonic reversal of the western Doruneh Fault System: implications for Central Asian tectonics. *Tectonics* **34**, 2034–51. https://doi.org/10.1002/2015TC003931

Jazi MA, Karimpour MH and Malekzadeh Shafaroudi A (2017) Nakhlak carbonate-hosted Pb-(Ag) deposit, Isfahan Province, Iran: a geological, mineralogical, geochemical, fluid inclusion, and sulfur isotope study. *Ore Geology Reviews* **80**, 27–47. https://doi.org/10.1016/j.oregeorev.2016.06.010

Jørgenson BB, Isaksen MF and Jannasch HW (1992) Bacterial sulfate reduction above 100°C in deep-sea hydrothermal vent sediments. *Science* **258**, 1756–57. https://doi.org/10.1126/science.258.5089.1756

Kesler SE (2005) Ore-forming fluids. *Elements* **1**, 13–8. https://doi.org/10.2113/gselements.1.1.13

Kharaka YK, Maest AS, Carothers WW, Law LM, Lamothe PJ and Fries TL (1987) Geochemistry of metal-rich brines from central Mississippi Salt Dome basin, U.S.A. *Applied Geochemistry* **2**, 543–61. https://doi.org/10.1016/0883-2927(87)90008-4

Kyle JR and Saunders JA (1996) Metallic deposits of the Gulf Coast basin, diverse mineralization styles in a young sedimentary basin. In *Carbonate-Hosted Lead-Zinc Deposits* (ed DF Sangster), pp. 218–29. Society of Economic Geologists, Special Publication no. 4.

Leach DL, Bradley D, Lewchuk MT, Symons DT, de Marsily G and Brannon J (2001) Mississippi Valley-type lead-zinc deposits through geological time: implications from recent age-dating research. *Mineralium Deposita* **36**, 711–40. https://doi.org/10.1007/s001260100208

Leach DL, Bradley DC, Huston D, Pisarevsky SA, Taylor RD and Gardoll SJ (2010a) Sediment-hosted lead-zinc deposits in earth history. *Economic Geology* **105**, 593–625. https://doi.org/10.2113/gsecongeo.105.3.593

Leach DL, Macquar JC, Lagneau V, Leventhal J, Emsbo P and Premo W (2006) Precipitation of lead-zinc ores in the Mississippi Valley-type deposit at Treves, cevennes region of southern France. *Geofluids* **6**, 24–44. https://doi.org/10.1111/j.1468-8123.2006.00126.x

Leach DL, Sangster DF, Kelley KD, Large RR, Garven G, Allen CR, Gutzmer J and Walters S (2005) Sediment-hosted Pb-Zn deposits: a global perspective. *Economic Geology 100th Anniversary*, pp. 561–608.

Leavitt WD, Halevy I, Bradley AS and Johnston DT (2013) Influence of sulfate reduction rates on the Phanerozoic sulfur isotope record. *Proceedings of the National Academy of Sciences* **110**, 11244–49. https://doi.org/10.1073/pnas.1218874110

Leven EJ and Gorgij MN (2006) Upper Carboniferous-Permian stratigraphy and fusulinids from the Anarak region, Central Iran. *Russian Journal of Earth Sciences* **8**, 1–25. https://doi.org/10.2205/2006ES000200

Li DF, Chen HY, Hollings P, Zhang L, Sun XM, Lu WJ, Wang CM and Fang J (2018) Isotopic footprints of the giant Precambrian Caixiashan Zn-Pb mineralization system. *Precambrian Research* **305**, 79–90. https://doi.org/10.1016/j.precamres.2017.11.014

Li ML, Liu SA, Xue CJ and Li D (2019) Zinc, Cadmium and sulfur isotope fractionation in a supergiant MVT deposit with bacteria. *Geochimica et Cosmochimica Acta* **265**, 1–18. https://doi.org/10.1016/j.gca.2019.08.018

Li Y and Liu J (2006) Calculation of sulfur isotope fractionation in sulfides. *Geochimica et Cosmochimica Acta* **70**, 1789–95. https://doi.org/10.1016/j.gca.2005.12.015

Liu JM and Liu JJ (1997) Basin fluid genetic model of sediment-hosted micro-disseminated gold deposits in the gold-triangle area between Guizhou, Guangxi and Yunnan. *Acta Mineralogica Sinica* **17**, 448–56 (in Chinese with English abstract).

Machel HG (1989) Relationships between sulphate reduction and oxidation of organic compounds to carbonate diagenesis, hydrocarbon accumulations, salt domes, and metal sulphide deposits. *Carbonates and Evaporites* **4**, 137–51.

Machel HG (2001) Bacterial and thermochemical sulfate reduction in diagenetic settings-old and new insights. *Sedimentary Geology* **140**, 143–75. https://doi.org/10.1016/S0037-0738(00)00176-7

Maghfouri S and Choulet F (2021) Ore-forming processes, O-C isotopes geochemistry, and fluid inclusions in the Darreh-Zanjir fault control MVT-type Zn-Pb deposit: Iran. *Arabian Journal of Geosciences* **14**, 2083. https://doi.org/10.1007/s12517-021-08469-2

Maghfouri S and Hosseinzadeh MR (2018) The early Cretaceous Mansourabad shale-carbonate hosted Zn-Pb (-Ag) deposit, central Iran: an example of vent-proximal sub-seafloor replacement SEDEX mineralization. *Ore Geology Reviews* **95**, 20–39. https://doi.org/10.1016/j.oregeorev.2018.02.020

Maghfouri S, Hosseinzadeh MR and Choulet F (2020a) Supergene nonsulfide Zn-Pb mineralization in the Mehdiabad world-class sub-seafloor replacement SEDEX-type deposit, Iran. *International Journal of Earth Sciences* **109**, 2531–55. http://dx.doi.org/10.1007/s00531-020-01916-7

Maghfouri S, Hosseinzadeh MR, Choulet F, Alfonso P, Azim Zadeh AM and Rajabi A (2019) Vent-proximal sub-seafloor replacement clastic-carbonate hosted SEDEX-type mineralization in the Mehdiabad world-class Zn-Pb-Ba-(Cu-Ag) deposit, southern Yazd Basin, Iran. *Ore Geology Reviews* **113**, 103047. https://doi.org/10.1016/j.oregeorev.2019.103047

Maghfouri S, Hosseinzadeh MR, Lentz DR and Choulet F (2020b) Geological and geochemical constraints on the Farahabad ventproximal ventproximal sub-seafloor replacement SEDEX-type deposit, southern Yazd basin, Iran. *Journal of Geochemical Exploration* **209**, 106436. https://doi.org/10.1016/j.gexplo.2019.106436

Maghfouri S, Hosseinzadeh MR, Lentz DR, Tajeddin HA, Movahednia M and Shariefi A (2021) Nature of ore-forming fluids in the Mehdiabad world-class sub-seafloor replacement SEDEX-type Zn-Pb-Ba-(Cu-Ag) deposit, Iran; constraints from geochemistry, fluid inclusions, and O-C-Sr isotopes. *Journal of Asian Earth Sciences* **207**, 104654. https://doi.org/10.1016/j.jseaes.2020.104654

Magnall JM, Gleeson SA, Stern RA, Newton RJ, Poulton SW and Paradis S (2016) Open system sulphate reduction in a diagenetic environment-isotopic analysis of barite ($\delta^{34}S$ and $\delta^{18}O$) and pyrite ($\delta^{34}S$) from the Tom and Jason Late Devonian Zn-Pb-Ba deposits, Selwyn Basin, Canada. *Geochimica et Cosmochimica Acta* **180**, 146–63. https://doi.org/10.1016/j.gca.2016.02.015

Mei Y, Sherman DM, Liu W, Etschmann B, Testemale D and Brugger J (2015) Zinc complexation in chloride-rich hydrothermal fluids (25-600 °C): a thermodynamic model derived from ab initio molecular dynamics. *Geochimica et Cosmochimica Acta* **150**, 265–84. https://doi.org/10.1016/j.gca.2014.09.023

Michalik M (1997) Chlorine containing illites, copper chlorides and other chloride bearing minerals in the Fore-sudetic copper deposit (Poland). In *Mineral Deposits: Research and Exploration* (ed H Papunen), pp. 543–6. Rotterdam: Balkema.

Mirnejad H, Simonetti A and Molasalehi F (2015) Origin and formational history of some Pb-Zn deposits from Alborz and Central Iran: Pb isotope constraints. *International Geology Review* **57**, 463–71. https://doi.org/10.1080/00206814.2015.1013510

Mudd GM, Jowitt SM and Werner TT (2017) The world's lead-zinc mineral resources: scarcity, data, issues and opportunities. *Ore Geology Reviews* **80**, 1160–90. https://doi.org/10.1016/j.oregeorev.2016.08.010

Nejadhadada M, Taghipour B and Lentz DR (2018) Geochemical, isotopic, and fluid inclusion signatures of Zn-Pb mineralization in the Tiran mining district, Isfahan, Sanandaj-Sirjan zone(Iran). *Ore Geology Reviews* **101**, 854–69. https://doi.org/10.1016/j.oregeorev.2018.08.005

Nozaem R, Mohajjel M, Rossetti F, Della Seta M, Vignaroli G, Yassaghi A, Salvini F and Eliassi M (2013) Post-Neogene right-lateral strike-slip tectonics at the north-western edge of the Lut Block (Kuh-e-Sarhangi Fault), Central Iran. *Tectonophysics* **589**, 220–33. https://doi.org/10.1016/j.tecto.2013.01.001

Ohmoto H (1972) Systematics of sulfur and carbon isotopes in hydrothermal ore deposits. *Economic Geology* **67**, 551–78. https://doi.org/10.2113/gsecongeo.67.5.551

Ohmoto H (1986) Stable isotope geochemistry of ore deposits. *Reviews in Mineralogy and Geochemistry* **16**, 491–560.

Ohmoto H and Goldhaber MB (1997) Sulfur and carbon isotopes. In *Geochemistry of Hydrothermal Ore Deposits*, 3rd edn (ed HL Barnes), pp. 517–611. New York: John Wiley and Sons.

Ohmoto H and Rye RO (1979) Isotopes sulfur and carbon. In *Geochemistry of Hydrothermal Ore Deposits*, 2rd edn. (ed HL Barnes), pp. 509–567. New York: John Wiley and Sons.

Pirajno F (2009) *Hydrothermal Processes and Mineral Systems*. Berlin: Springer, 1250 pp.

Pirajno F (2013) *The Geology and Tectonic Setting of China's Mineral Deposits*. Berlin: Springer, 682 pp.

Plumlee GS, Leach DL, Hofstra AH, Landis GP, Rowan EL and Viets JG (1994) Chemical reaction path modeling of ore deposition in Mississippi Valley-type Pb-Zn deposits of the Ozark region, U.S. midcontinent. *Economic Geology* **89**, 1361–83. https://doi.org/10.2113/gsecongeo.89.6.1361

Rajabi A, Alfonso P, Canet C, Rastad E, Niroomand S, Modabberi S and Mahmoodi P (2020) The world-class Koushk Zn-Pb deposit, Central Iran: a genetic model for vent-proximal shale-hosted massive sulfide (SHMS) deposits-based on paragenesis and stable isotope geochemistry. *Ore Geology Reviews* **124**, 103654. https://doi.org/10.1016/j.oregeorev.2020.103654

Rajabi A, Canet C, Alfonso P, Mahmoodi P, Yarmohammadi A, Sharifi S, Mahdavi A and Rezaei S (2022) Mineralization and structural controls of the AB-Bid carbonate-hosted Pb-Zn (±Cu) deposit, Tabas-Posht e Badam Metallogenic Belt, Iran. *Minerals* **12**, 95. https://doi.org/10.3390/min12010095

Rajabi A, Canet C, Rastad E and Alfonso P (2015) Basin evolution and stratigraphic correlation of sedimentary-exhalative Zn-Pb deposits of the Early Cambrian Zarigan-Chahmir Basin, Central Iran. *Ore Geology Reviews* **64**, 328–53. https://doi.org/10.1016/j.oregeorev.2014.07.013

Rajabi A, Rastad E and Canet C (2012) Metallogeny of Cretaceous carbonate hosted Zn-Pb deposits of Iran: geotectonic setting and data integration for future mineral exploration. *International Geology Review* **54**, 1649–72. https://doi.org/10.1080/00206814.2012.659110

Rajabi A, Rastad E and Canet C (2013) Metallogeny of Permian-Triassic carbonatehosted Zn-Pb and F deposits of Iran: a review for future mineral exploration. *Australian Journal of Earth Sciences* **60**, 197–216. https://doi.org/10.1080/08120099.2012.754792

Ramezani J and Tucker RD (2003) The Saghand Region, Central Iran: U-Pb geochronology, petrogenesis and implication for Gondwana tectonics. *American Journal of Science* **303**, 622–65. https://doi.org/10.2475/ajs.303.7.622

Reed MH (2006) Sulfide mineral precipitation from hydrothermal fluids. *Reviews in Mineralogy and Geochemistry* **61**, 609–31. https://doi.org/10.2138/rmg.2006.61.11

Rees CE (1973) A steady-state model for sulfur isotope fractionation in bacterial reduction processes. *Geochimica et Cosmochimica Acta* **37**, 1141–62. https://doi.org/10.1016/0016-7037(73)90052-5

Reynolds NA and Large D (2010) Tethyan zinc-lead metallogeny in Europe, North Africa, and Asia. *Society of Economic Geologists Special Publication* **15**, 339–65.

Roedder E (1984) *Fluid inclusions. Reviews in Mineralogy* 12, Mineralogical Society of America, 644 pp.

Ruaya JR and Seward TM (1986) The stability of chlorozinc (II) complexes in hydrothermal solutions up to 350 °C. *Geochimica et Cosmochimica Acta* **50**, 651–61. https://doi.org/10.1016/0016-7037(86)90343-1

Sangster DF (1990) Mississippi Valley-type and Sedex lead-zinc deposits: a comparative examination. *Transactions of the Institution of Mining and Metallurgy-Section B* **99**, B21–42.

Sangster DF, Outridge PM and Davis WJ (2000) Stable lead isotope characteristics of lead ore deposits of environmental significance. *Environmental Reviews* **8**, 115–47. https://doi.org/10.1139/er-8-2-115

Sawicka JE, Jørgensen BB and Brüchert V (2012) Temperature characteristics of bacterial sulfate reduction in continental shelf and slope sediments. *Biogeosciences* **9**, 3425–35. https://doi.org/10.5194/bg-9-3425-2012

Seal RR (2006) Sulfur isotope geochemistry of sulfide minerals. *Reviews in Mineralogy and Geochemistry* **61**, 633–77. https://doi.org/10.2138/rmg.2006.61.12

Seward TM (1976) The stability of chloride complexes of silver in hydrothermal solutions up to 350 °C. *Geochimica et Cosmochimica Acta* **40**, 1329–41. https://doi.org/10.1016/0016-7037(76)90122-8

Seward TM, Williams-Jones AE and Migdisov AA (2014) The chemistry of metal transport and deposition by ore-forming hydrothermal fluids. *Treatise on Geochemistry* **13**, 29–57. https://doi.org/10.1016/b978-0-08-095975-7.01102-5

Shepherd TJ, Rankin AH and Aiderton DHM (1985) *A Practical Guide to Fluid Inclusion Studies*. Blackie and Son Limited, 239 pp.

Sicree AA and Barnes HL (1996) Upper Mississippi Valley district ore fluid model: the role of organic complexes. *Ore Geology Reviews* **11**, 105–31. https://doi.org/10.1016/0169-1368(95)00018-6

Sim MS, Bosak T and Ono S (2011) Large sulfur isotope fractionation does not require disproportionation. *Science* **333**, 74–7. https://doi.org/10.1126/science.1205103

Song Y, Hou Z, Liu Y and Zhang H (2017) Mississippi Valley-Type (MVT) Pb-Zn deposits in the Tethyan domain. *Geology in China* **44**, 664–89. https://doi.org/10.12029/gc20170403

Song Y, Liu Y, Hou Z, Fard M, Zhang H and Zhuang L (2019) Sediment-Hosted Pb–Zn deposits in the Tethyan domain from China to Iran: Characteristics, tectonic setting, and ore controls. *Gondwana Research* **75**, 249–81. https://doi.org/10.1016/j.gr.2019.05.005

Spangenberg J, Fontboté L, Sharp ZD and Hunziker J (1996) Carbon and oxygen isotope study of hydrothermal carbonates in the zinc-lead deposits of the San Vicente District, Central Peru: a quantitative modeling on mixing processes and CO_2 degassing. *Chemical Geology* **133**, 289–315. https://doi.org/10.1016/S0009-2541(96)00106-4

Stöcklin J (1968) Structural history and tectonics of Iran; a review. *American Association of Petroleum Geologists Bulletin* **52**, 1229–58. https://doi.org/10.1306/5D25C4A5-16C1-11D7-8645000102C1865D

Stöcklin J (1974) Possible ancient continental margins in Iran. In *The Geology of Continental Margins* (eds CA Burke and CL Drake), pp. 873–87. New York: Springer-Verlag.

Sverjensky DA (1981) The origin of a Mississippi Valley-type deposit in the Viburnum Trend, Southeast Missouri. *Economic Geology* **76**, 1848–72. https://doi.org/10.2113/gsecongeo.76.7.1848

Sverjensky DA (1986) Genesis of Mississippi Valley-type lead-zinc deposits. *Annual Review of Earth and Planetary Sciences* **14**, 177–99. https://doi.org/10.1146/annurev.ea.14.050186.001141

Sverjensky DA (1989) Chemical evolution of basinal brines that formed sediment hosted Cu-Pb-Zn Deposits. In *Sediment-Hosted Stratiform Copper Deposits* (eds RW Boyle, AC Brown, CW Jefferson, EC Jowett and RV KirKham), pp. 127–34. Geological Association of Canada, Special Paper no. 36.

Sverjensky DA, Shock EL and Helgeson HC (1997) Prediction of the thermodynamic properties of aqueous metal complexes to 1000 °C and 5 kb. *Geochimica et Cosmochimica Acta* **61**, 1359–412. https://doi.org/10.1016/s0016-7037(97)00009-4

Tagirov BR and Seward TM (2010) Hydrosulfide/sulfide complexes of zinc to 250 °C and the thermodynamic properties of sphalerite. *Chemical Geology* **269**, 301–11. https://doi.org/10.1016/j.chemgeo.2009.10.005

Tagirov BR, Suleimenov OM and Seward TM (2007) Zinc complexation in aqueous sulfide solutions: determination of the stoichiometry and stability of complexes via $ZnS_{(cr)}$ solubility measurements at 100 °C and 150 bars. *Geochimica et Cosmochimica Acta* **71**, 4942–953. https://doi.org/10.1016/j.gca.2007.08.012

Takahashi T (1960) Supergene alteration of zinc and lead deposits in limestone. *Economic Geology* **55**, 1083–115. https://doi.org/10.2113/gsecongeo.55.6.1083

Taylor JHP, Frechen J and Degens ET (1967) Oxygen and carbon isotope studies of carbonatites from the Laacher See District, West Germany and the Alnö District Sweden. *Geochimica et Cosmochimica Acta* **31**, 407–30. https://doi.org/10.1016/0016-7037(67)90051-8

Taylor SR and McLennan SM (1985) *The Continentalcrust: Its Composition and Evolution: An Examination of the Geochemical Record Preserved in Sedimentary Rocks*. Oxford: Blackwell Scientific, 312 pp.

Torabi G (2010) Early Oligocene alkaline lamprophyric dykes from the Jandaq area(Isfahan Province, Central Iran): evidence of Central-East Iranian microcontinent confining oceanic crust subduction. *Island Arc* **19**, 277–91. https://doi.org/10.1111/j.1440-1738.2009.00705.x

Torabi G (2011) Late Permian blueschist from Anarak ophiolite (Central Iran, Isfahan province), a mark of multi-suture closure of the Paleo-Tethys ocean. *Revista Mexicana de Ciencias Geologicas* **28**, 544–54.

Torabi G. 2012. Late Permian post-ophiolitic trondhjemites from Central Iran: a mark of subduction role in growth of Paleozoic continental crust. *Island Arc* **21**, 215–29. https://doi.org/10.1111/j.1440-1738.2012.00817.x

Van den Kerkhof AM and Hein UF (2001) Fluid inclusion petrography. *Lithos* **55**, 27–47. https://doi.org/10.1016/s0024-4937(00)00037-2

Veizer J and Hoefs J (1976) The nature of $^{18}O/^{16}O$ and $^{13}C/^{12}C$ secular trends in sedimentary carbonate rocks. *Geochimica et Cosmochimica Acta* **40**, 1387–95. https://doi.org/10.1016/0016-7037(76)90129-0

Wang LJ, Mi M, Zhou JX and Luo K (2018) New constraints on the origin of the Maozu carbonate-hosted epigenetic Zn-Pb deposit in NE Yunnan Province, SW China. *Ore Geology Reviews* **101**, 578–94. https://doi.org/10.1016/j.oregeorev.2018.08.012

Warr LM (2021) IMA–CNMNC approved mineral symbols. *Mineralogical Magazine* **85**, 291–320. https://doi.org/10.1180/mgm.2021.43

Wellman HW (1966) Active wrench faults of Iran, Afghanistan and Pakistan. *International Journal of Earth Sciences* **55**, 716–35. https://doi.org/10.1007/BF02029650

Wendt J, Kaufmann B, Belka Z, Farsan N and Bavandpur AK (2005) Devonian/Lower Carbonifeous stratigraphy, facies patterns and palaeogeography of Iran Part I. Northern and Central Iran. *Acta Geologica Polonica* **52**, 129–68.

Wilkinson JJ (2001) Fluid inclusions in hydrothermal ore deposits. *Lithos* **55**, 229–72. https://doi.org/10.1016/S0024-4937(00)00047-5

Wilkinson JJ (2014) Sediment-hosted zinc-lead mineralization: processes and perspectives. In *Treatise on Geochemistry,* 2rd edn (eds HD Holland and KK Turekian), pp. 219–49.

Wilmsen M, Fürsich FT, Seyed-Emami K, Majidifard MR and Taheri J (2009) The Cimmerian orogeny in northern Iran: tectono-stratigraphic evidence from the foreland. *Terra Nova* **21**, 211–18. https://doi.org/10.1111/j.1365-3121.2009.00876.x

Worden RH, Smalley PC and Oxtoby NH (1995) Gas souring by the thermochemical sulphate reduction at 140°C. *American Association of Petroleum Geologists Bulletin* **79**, 854–63.

Zanchetta S, Malaspina N, Zanchi A, Benciolini L, Martin S, Javadi HR and Kouhpeyma M (2017) Contrasting subduction-exhumation paths in the blueschists of the Anarak Metamorphic Complex (Central Iran). *Geological Magazine* **155**, 316–34. https://doi.org/10.1017/S0016756817000218

Zanchi A, Malaspina N, Zanchetta S, Berra F, Benciolini L, Bergomi M, Cavallo A, Javadi HR and Kouhpeyma M (2015) The Cimmerian accretionary wedge of Anarak, Central Iran. *Journal of Asian Earth Sciences* **102**, 45–72. https://doi.org/10.1016/j.jseaes.2014.08.030

Zanchi A, Zanchetta S, Garzanti E, Balini M, Berra F, Mattei M and Muttoni G (2009) The Cimmerian evolution of the Nakhlak-Anarak area, Central Iran and its bearing for the reconstruction of the historyof the Eurasian margin. In *South Caspian to Central Iran Basins* (eds MF Brunet, M Wilmsen and JW Granath), pp. 31–55. Geological Society of London, Special Publication no. 312.

Zartman RE and Doe BR (1981) Plumbotectonics-the model. *Tectonophys* **75**, 135–62. https://doi.org/10.1016/0040-1951(81)90213-4

Zheng YF (1999) Oxygen isotope fractionation in carbonate and sulfate minerals. *Geochemical Journal* **33**, 109–26. https://doi.org/10.2343/geochemj.33.109

Zhong R, Brugger J, Chen YJ and Li WB (2015) Contrasting regimes of Cu, Zn and Pb transport in ore-forming hydrothermal fluids. *Chemical Geology* **395**, 154–64. https://doi.org/10.1016/j.chemgeo.2014.12.008